A PANEL-FREE METHOD FOR TIME-DOMAIN ANALYSIS OF FLOATING BODIES IN WAVES

by

Wei Qiu

Submitted
in partial fulfillment of the requirements
for the degree of

DOCTOR OF PHILOSOPHY

Major Subject: Naval Architecture

at

DALHOUSIE UNIVERSITY

Halifax, Nova Scotia June 2001

0-612-63483-3

Dalhousie University

Faculty of Engineering

The undersigned hereby certify that they have examined, and recommend to the Faculty of Graduate Studies for acceptance, the thesis entitled "A Panel-Free Method for Time-Domain Analysis of Floating Bodies in Waves" by Wei Qiu in partial fulfillment of the requirements for the degree of Doctor of Philosophy.

Dated: June 20, 2001

Supervisor: [redacted]
C.C. Hsiung

External Examiner: [redacted]
S. Calisal
University of British Columbia
Canada

Examiners: [redacted]
A. Kalamkarov

[redacted]
G. Fenton

Dalhousie University
Faculty of Engineering

DATE: June 20, 2001

AUTHOR: Wei Qiu

TITLE: A Panel-Free Method for Time-Domain Analysis of Floating Bodies in Waves

MAJOR SUBJECT: Mechanical Engineering/Naval Architecture

DEGREE: DOCTOR OF PHILOSOPHY

CONVOCATION: October 2001

[redacted]

[redacted] Signature of Author

TABLE OF CONTENTS

List of Tables

List of Figures

NOMENCLATURE

$F(P,Q;t-\tau)$	wave part of the Green function
$G(P,Q;t-\tau)$	time-dependent Green function
$G_0(P,Q)$	Rankine source
$H(t-\tau)$	Heaviside unit step function
J_0	Bessel function of order zero
$K_{j7}^D(t)$	response function for the diffraction force in the jth direction
$K_{jk}^R(t)$	response function of the floating body due to the radiated waves
$N_{i,p}$ and $N_{j,q}$	normalized B-spline basis functions
$S_f(t)$	free surface
$S_b(t)$	instantaneous wetted surface of the body
$\bar{S}_b$	mean wetted surface of the ship
$\bar{S}_b'$	image of the body surface $\bar{S}_b$

S_∞	infitnity spatial boundary
$\mathbf{U}$	knot vector used for the NURBS surface
U_0	forward speed
$\mathbf{V}_s(P;t)$	velocity on the body surface at the point $P(x,y,z)$ at time t
$V_n(P;t)$	normal velocity on the body surface at the point P at time t
$\mathbf{W}$	steady flow velocity vector
g	acceleration of gravity
k	wave number (except when used as a subscript)
m_k	m-terms which are the gradients of the steady velocity in the normal direction
$\mathbf{n}$	unit inner normal into the body surface
$p(P;t)$	pressure at a point P at time t
r and r_1	distance between the source and field points
$\mathbf{r}_g$	position vector for CG
t	time
t_0	initial time
x_g, y_g, z_g	coordinates of the centre of gravity in the ship-fixed coordinate system
Γ	intersection of the hull surface and the calm water plane

$\Phi(P;t)$	total velocity potential at the point $P(x,y,z)$ at time t
Φ^{db}	double-body potential function
$\bar{\Phi}(P)+\bar{\phi}$	velocity potential due to the steady translation
Ω	fluid domain
α	arbitrary constant to control the non-impulsive input motion
β	heading angle of wave propagation relative to the x-axis (180^0 denotes head seas)
$\gamma(P)$	source strength which makes the body surface an equipotential surface
$\bar{\gamma}_{jk}$	coefficient of hydrodynamic restoring force in the time domain
$\delta(t-\tau)$	Dirac delta function
η	free surface elevation
$\bar{\eta}_0(t)$	non-impulsive incident wave at the origin of the steady-moving coordinate system
$\eta_0(t)$	free surface elevation of the incident wave at the origin of the steady-moving coordinate system
$\bar{\lambda}_{jk}$	hydrodynamic damping coefficient in the time domain
$\bar{\mu}_{jk}$	added-mass of the floating body in the time domain
ρ	fluid density

$\sigma(Q;\tau)$	source strength
ϕ_0	constant potential for an equipotential surface
$\nabla\bar{\phi}_0(P;t)$	spatial derivatives of the non-impulsive incident wave potential
ϕ_D or ϕ_7	diffracted wave potential
ϕ_I	incident wave potential
ϕ_k	radiated wave potential in kth mode
ψ_k, $\bar{\chi}_k$, φ_k	potential components due to the input motion
ω	wave frequency
ω_e	frequency of encounter

ACKNOWLEDGMENTS

Many people have in various ways contributed to this work to whom I would like to thank individually. I would like to give my foremost appreciation and thanks to my supervisor, Professor C.C. Hsiung who has greatly enhanced my interest in Marine Hydrodynamics, for his continuous academic guidance with patience, kindness, encouragement, and support throughout this thesis work. The discussions with him were always inspiring. His advice and guidance have been invaluable to the development of this work.

Many thanks are extended to Professor J.M. Chuang for his comments and interests in my research, and also for his kind support on the UNIX computing system. I also would like to acknowledge advice and comments from Professor A. Kalamkarov and Professor G. Fenton. I am also indebted to Mr. Sam Ando of Defence Research Establishment Atlantic (DREA), for his various suggestions on this research work. Participating in the contract work with DREA has strengthened my research experience, especially in the time-domain analysis of ship motion. I treasure this experience very much.

My special thanks are extended to my former senior colleague, Dr. L.Z. Cong, at the

Centre for Marine Vessel Development and Research, Dalhousie University for useful discussions in developing this thesis.

I would like to express my deep appreciation for the support from Martec Limited during my last phase of Ph.D. study. Special appreciations are extended to Dr. Michael W. Chernuka for his understanding, encouragement and advice on this work. This work was supported by the Natural Sciences and Engineering Research Council of Canada (NSERC). Without the NSERC support, this work could never be possibly completed. I would also like to thank the support of the Reid Scholarship, the Bruce and Dorothy Rosetti Engineering Research Scholarship and the Faculty of Engineering Scholarship, Dalhousie University.

Finally, I am profoundly grateful to my wife, Hongxuan Peng, for her love, support, patience and understanding throughout my studies and research. Her standing at my side has made this work a very enjoyable endeavor that I will remember fondly. I would like to express my appreciation to my son, Christopher, who even was not aware of my work. He was very cooperative during my preparation of this document. I am also indebted to my Mother-in-Law, Shuzhen Dong, who was able to keep little Christopher at bay at the critical moments.

ABSTRACT

A panel-free method (PFM) has been developed to solve the radiation and the diffraction problems of floating bodies in the time domain. The velocity potentials due to non-impulsive inputs are obtained by solving the boundary integral equations in terms of source strength distribution. The singularity in the Rankine source of the time-dependent Green function is removed. The geometry of a body surface is mathematically represented by NURBS surfaces. The integral equation can be globally discretized over the body surface by Gaussian quadratures. No assumption is needed for the degree of approximation of distributed source strength on the body surface.

The accuracy of PFM was first demonstrated by its application to a classical problem of uniform flow past a sphere. The radiation and diffraction response functions of a hemisphere at zero speed were then computed by PFM. The PFM was also applied to a Wigley hull. The computed response functions, added-mass and damping coefficients, and the diffraction forces for the hemisphere and the Wigley hull were compared with published results.

Compared with the panel method, the advantages of PFM are: a) less numerical manipulation, since panelization of a body surface is not needed; b) more accurate, since the assumption for the degree of approximation of source strength distribution as in the panel method is not needed and the surface geometry can be described mathematically. c) the integral equation is desingularized before it is discretized so that Gaussian quadrature can be applied directly and globally. d) the Gaussian quadrature points, and their respective Jacobian and normals on the surface can be accurately computed based on the NURBS expression; and e) the accuracy of the solution can be easily controlled by changing the number and/or the arrangement of Gaussian quadrature points.

Chapter 1

Introduction

1.1 Panel Methods

The predictions of wave-induced motions, loads and hydrodynamic pressures over a ship hull are essential elements of ship design. Over the past few decades computational hydrodynamics has been developed as a powerful tool for both ocean engineers and naval architects. It allows evaluation of preliminary designs or ship performance at a relatively low cost compared with experimental tests.

The potential flow theory has been widely used in marine hydrodynamics. It is mathematically attractive and physically appropriate. For a floating body in waves, the initial-boundary-value-problem can be described by Laplace's equation subject to the free surface conditions, body boundary conditions, bottom conditions, far field conditions, and appropriate initial conditions. An integral equation for the initial-boundary-value-problem can be derived by applying Green's theorem and it can be solved numerically by various methods.

Strip theory was applied as the first analytical ship motion theory for computations and has been used as a practical prediction method, but it gives unsatisfactory predictions at low frequencies and at high forward speeds, and it is not applicable to ships of low length-beam ratios due to its slender body assumptions. Also, the strip-theory approach is not able to compute the hydrodynamic pressure distribution over the hull surface except on sections. Some of the deficiencies of strip theory can be removed by the three-dimensional flow theory. Hess and Smith (1964) pioneered the panel method, where a source distribution was developed for flows without a free surface, which are equivalent to double-body flows with a rigid free surface. The body surface was subdivided into a number of flat quadrilaterals over which the source strength was assumed to be constant. The body boundary conditions were satisfied at the center of each quadrilateral. A system of N linear equations resulted from the boundary integral equation for unknown source strengths. The potential, velocities and the pressure at the centroid of each panel can then be determined from the source strength. Since the singularity solution of integration can be obtained by using planar quadrilateral panels or triangles and constant source strength over a panel, the constant-source-flat-panel method has been used in a wide variety of problems both in the frequency domain and the time domain. In the case that the free surface has to be taken into account, the free surface Green function is applied to automatically satisfy the linearized radiation and diffraction free surface conditions and the far field boundary conditions. The body boundary conditions are enforced on the panels. It is often referred as a *lower-order* panel method. Normally, a large number of panels are required to achieve accurate results. In many applications, such as computation of second-order forces, the lower-order panel method fails to provide accurate gradient of velocity potential.

Higher-order panel methods have been developed in various degrees to overcome the deficiencies of the constant-source-flat-panel method by improvement of geometric approximation and/or source distribution methods. Most higher-order methods allow for linear or quadratic panels and first- or second-degree polynomial distribution of source strength over a panel. It normally requires more computational effort than the lower-order panel method. Hsin (1993) and Maniar (1995) applied B-splines and developed a higher-order panel method in which the potential and the geometry of a body are allowed any degree of continuity. Recently, Lee *et al.* (1998) and Danmeier (1999) have presented a geometry-independent higher-order method which separates the geometric and hydrodynamic representations. The velocity potential is described by B-splines. It allows for accurate geometry description and flexibility of potential discretization.

The present thesis is aimed at developing a state-of-the-art numerical tool to reduce the computational error of the panel method due to the geometrical approximation and also the assumption of the degree of approximation of the source strength distribution.

1.2 Time-Domain Simulation

Several researchers, such as Chang (1977), Inglis and Price (1982) and Guevel and Bougis (1982), have used three-dimensional panels to obtain solutions of ship motion in the frequency domain. But the computational results based on the Green function with forward velocity were never satisfactory, due to the complication caused by the forward speed term. The frequency-domain panel method has been employed for ship seakeeping analysis using zero-speed Green function with a "speed correction". An alternative approach is to formulate the ship motion problem directly in the time domain. When the forward speed is involved, the time-domain Green function is in a simpler form and requires less computational effort than does the frequency-domain counterpart.

The concept of direct time-domain solution is based on the early work of Finkelstein (1957), Stoker (1957) and Wehausen and Laitone (1960). Cummins (1962) and Ogilvie (1964) discussed the use of time-domain analysis to solve unsteady ship motion problems. The zero forward speed problem has been discussed in detail by Wehausen (1967, 1971).

In the linear time-domain formulation, the time-dependent Green function is applied to derive a boundary integral equation at the mean wetted surface of the body under the assumptions of small body motion and small amplitude incident waves. The linearized radiation and diffraction forces acting on the body can be expressed in terms of convolution integrals of the arbitrary motion with impulse functions. These methods have been developed by Liapis and Beck (1985), Beck and Liapis (1987), Beck and King (1989), Beck and Magee (1990), Lin and Yue (1994). Based on the work of de Kat (1990) who computed the Froude-Krylov forces on the instantaneous surfaces, a combined time-domain simulation scheme has been developed by Cong *et al.* (1998) and Qiu *et al.* (2000) to take into account the nonlinear effect of the incident waves. In their work, the radiation and diffraction forces were computed at the mean wetted surface by applying the impulse response function. The Froude-Krylov and restoring forces were computed at the instantaneous wetted surface under the incident wave profile. The other nonlinear forces such as maneuvering force, rudder force and viscous damping force were also considered. To enhance the capability of the combined formulation, a pseudo-nonlinear scheme was investigated in the work of Seibert (2000) and Qiu *et al.* (2001a, 2001b) by considering the varied hydrodynamic coefficients for various waterlines. In their work, the time-domain added-mass, damping and restoring force coefficients were pre-computed for respective wetted surfaces with chosen hull attitudes and then were interpolated at the instantaneous wetted surface at each time step. This method showed promising improvement of motion prediction, particularly for roll. However, additional efforts are needed to panelize the hull for various positions.

Efforts have been made to directly incorporate nonlinearity into time-domain formulation. One extension of the linear time-domain model is to impose the body boundary condition on the instantaneous wetted surface of the body. The free surface boundary condition remains linear so that the time-dependent Green function can still be applied. The body-exact problem has been solved with various degrees of success by Lin and Yue (1990), Magee (1994) and Danmeier (1999). Huang (1997) combined the exact body boundary condition with a free-surface condition linearized about the incident wave profile. In the results of these studies, the application of the exact body boundary conditions showed promise of improvement for cases of computations dealing with large-amplitude motions.

1.3 Desingularization of the Integral Equation

In the higher-order panel methods, the singular $1/r$ term can be evaluated numerically in a variety of ways. For example, Beck *et al.* (1994) separated the integration and control surfaces; and the solution was obtained by integrating a distribution of singularities over a surface outside the fluid domain. In the work of Danmeier (1999), an adaptive subdivision and triangulation scheme was used to evaluate the singularity of the free-surface Green function.

Landweber and Macagno (1969) proposed a desingularized procedure which removed the singularity of $1/r$ *before* discretizing the integral equation and applied it to the problem of uniform flow past an ellipsoid. The numerical solution then could be applied to the exact boundary geometry, and the integral equation could be discretized over the body surface by Gaussian quadratures. Theoretically, this eliminates the errors due to both the geometrical approximation and the assumed degree of approximation of source strength distribution in the panel method. Kouh and Ho (1996) further developed this method and applied it to solve problems of uniform flow past a sphere, an ellipsoid and a Wigley hull in which geometries were represented by analytical expressions. Recently, Qiu and Hsiung (2000, 2001) have developed a desingularization scheme for the time-domain analysis. In their work, the Non-Uniform Rational B-Splines (NURBS) were adopted to described the body geometry so that the desingularization method can be applied to arbitrary bodies.

1.4 Large-Amplitude Motion Analysis

As mentioned above, to simulate the large-amplitude motion of floating bodies in waves, the body-exact problem can be applied and solved on the instantaneous wetted surface with the application of the time-domain Green function. This will require trimming and re-panelization at each time step. However, there are difficulties to develop a practical, efficient and automatic panel generator, especially for complex geometries. Furthermore, effort has also to be made to treat the singularities if a higher-order panel method is employed. Therefore, the other aim of this thesis is to report fundamental research in developing a tool for the time-domain simulation to solve a desingularized integral equation which can avoid re-panelization, and reduce the time for numerical integration, and provide easy control on the accuracy of solutions.

1.5 Thesis Contents

The scope of this thesis includes the development of a panel-free method and its applications to the time-domain analysis of floating bodies in waves. A panel-free method (PFM) has been developed to solve the radiation and the diffraction problems of floating bodies by employing the response function method in the time domain. A desingularized integral equation in terms of source strength distribution has been developed to remove the singularity in the time-dependent Green function. The velocity potentials due to a non-impulsive input were computed for the radiation and diffraction problems by solving the desingularized boundary integral equations. The geometry of a body surface was mathematically represented by Non-Uniform Rational B-Splines (NURBS) surfaces. The integral equation can then be globally discretized over the body surface by Gaussian quadratures. No assumption was needed for the degree of approximation of distributed source strength on the body surface.

In comparison with panel methods, the advantages of PFM have been proven to be: a) less numerical manipulation, since panelization of a body surface is not needed; b) greater accuracy, since the assumption for the degree of approximation of source strength distribution as in the panel method is not needed and surface geometry can be mathematically described; c) the integral equation is desingularized before it is discretized so that Gaussian quadrature can be applied directly and globally. In the panel method, the singularity remains in the discretized integral equation and Gaussian quadrature cannot be applied directly over the body surface; d) the Gaussian quadrature points, and their respective Jacobian and normals on the surface can be accurately computed based on NURBS expression; The NURBS surface can be obtained directly from commercial computer-aided-design packages; and e) the accuracy of the solution can be easily controlled by changing the number and/or the arrangement of Gaussian quadrature points.

The initial-boundary-value problem, its associated boundary integral equations for radiation and diffraction problems in the time domain and solutions by the impulse response function method are stated in Chapter 2. Chapter 3 describes the desingularization of integral equations, the NURBS representation of the body geometry numerical implementation of the panel-free method. Results demonstrating the accuracy of PFM are presented in Chapter 4. The application of PFM to a hemisphere and a Wigley hull was demonstrated. The computed response functions, added-mass and damping coefficients, and the diffraction forces and wave exciting forces were compared with published results.

Conclusions and recommendations for future research are presented in Chapter 5.

Chapter 2

Time-Domain Formulation

2.1 Coordinate Systems

Three right-handed coordinate systems (as shown in Figure 2.1) are employed for the time-domain analysis of floating bodies in waves. A *space-fixed* coordinate system, $OXYZ$, has the OXY plane coinciding with the undisturbed water surface and the Z-axis pointing vertically upward. In the *steady-moving* coordinate system, $o_m x_m y_m z_m$, the $o_m x_m y_m$ plane coincides with the calm water surface and $o_m z_m$ is positive upward. The third coordinate system, $oxyz$, is fixed on the floating body, and o is at the point of intersection of calm water surface, the longitudinal plane of symmetry, and the vertical plane passing through the midsection of the floating body. The oxy plane coincides with the undisturbed water surface when the body is at rest. The positive x-axis points toward the bow and the y-axis to the port side.

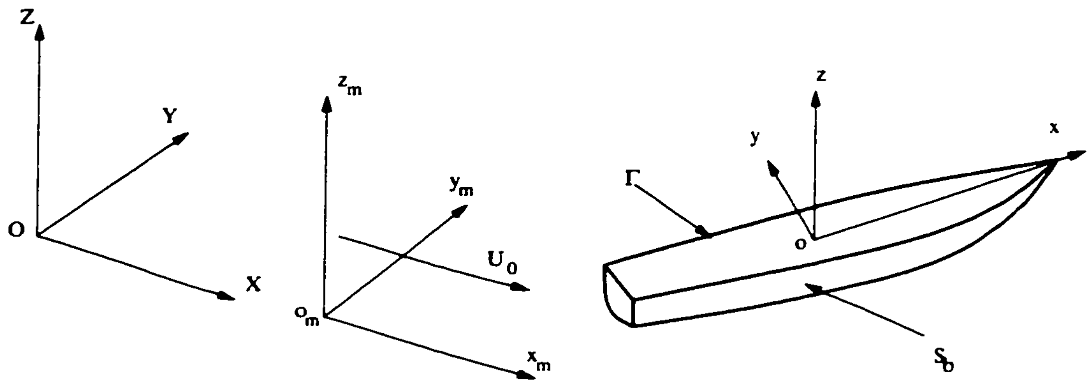

Figure 2.1: Coordinate systems

Denoting a column vector by braces $\{\}$, motions in the $o_m x_m y_m z_m$ system are represented by the vector $\mathbf{X}_m = \{x_{m_1}, x_{m_2}, x_{m_3}, x_{m_4}, x_{m_5}, x_{m_6}\}$, in which $\{x_{m_1}, x_{m_2}, x_{m_3}\}$ are the displacements of the center of gravity (CG), and $\{x_{m_4}, x_{m_5}, x_{m_6}\}$ are the Eulerian angles of the body. The Eulerian angles are the measurements of the body's rotation about the axes which pass through the CG of the body. The instantaneous translational velocities of body motion in the directions of ox, oy and oz are $\{\dot{x}_1, \dot{x}_2, \dot{x}_3\}$, and the rotational velocities about axes parallel to ox, oy and oz and passing through CG are $\{\dot{x}_4, \dot{x}_5, \dot{x}_6\}$.

2.2 The Initial Boundary Value Problem

It is assumed that the fluid is incompressible, inviscid and free of surface tension and that the flow is irrotational. Consider a three-dimensional body in a semi-infinite fluid with a free surface. The floating body moves in an incident wave field with a constant speed U_0 and is allowed to perform small unsteady oscillations about its mean positions in six degrees of freedom.

Under the above assumptions, the fluid velocity of a point $P(x, y, z)$ at time t can be described by the gradient of a scalar velocity potential,

$$\mathbf{V}(P;t) = \nabla\Phi(P;t) \tag{2.1}$$

Conservation of mass requires that the velocity potential satisfies Laplace equation in the fluid domain Ω,

$$\nabla^2\Phi(P;t) = 0 \tag{2.2}$$

The pressure $p(P;t)$ in the fluid is given by Bernoulli's equation,

$$p(P;t) = -\rho(\Phi_t + \frac{1}{2}|\nabla\Phi|^2 + gz_0) + p_a \tag{2.3}$$

where g is the acceleration of gravity; ρ is the fluid density; z_0 is the z-coordinate of a point on the free surface; p_a is the constant atmosphere pressure; Φ_t denotes the partial differentiation of Φ with respect to time t. Subject to the assumption that the surface tension and viscous effect are neglected and $p_a = 0$, the exact boundary condition on the free surface $S_f(t)$ can be written as

$$\Phi_{tt} + 2\nabla\Phi \cdot \nabla\Phi_t + \frac{1}{2}\nabla\Phi \cdot \nabla(\nabla\Phi \cdot \nabla\Phi) + g\Phi_{z_0} = 0, \quad \text{on } z_0 = \eta \tag{2.4}$$

where (x_0, y_0, z_0) defines a point on the free surface and $\eta(x_0, y_0; t)$ is the unknown free surface elevation, and Φ_{z_0} denotes the partial differentiation of Φ with respect to z_0. Two initial conditions are

$$\left.\begin{aligned} \Phi &= 0 \\ \Phi_t &= 0 \end{aligned}\right\} \quad \text{on } z_0 = 0,\ t \leq t_0 \tag{2.5}$$

where t_0 is the starting time for the fluid motions which is zero in the radiation problem and $-\infty$ in the diffraction problem.

On the submerged surface of the floating body, the no flux body-boundary condition must be satisfied,

$$(\nabla\Phi - \mathbf{V}_s) \cdot \mathbf{n} = 0 \quad \text{on } S_b(t) \tag{2.6}$$

where $\mathbf{V}_s(P; t)$ is the velocity at the point $P(x, y, z)$ on the body surface; $\mathbf{n}$ is the unit inner normal vector pointing into the body surface; and $S_b(t)$ is the instantaneous wetted surface of the body. Fluid motions caused by the body will go to zero at spatial infinity, S_∞, for all finite time,

$$\nabla\Phi \to 0, \quad R_1 = \sqrt{x^2 + y^2} \to \infty, \quad \text{for } t < \infty \tag{2.7}$$

2.3 Linearization

Both the free surface and the body boundary conditions, as well as the Bernoulli equation can be linearized. It is assumed that the fluid perturbations due to the steady forward motion and the unsteady oscillations are small and then the linear superposition can be applied. The total velocity potential can be expressed as follows:

$$\Phi(P;t) = \bar{\Phi}(P) + \bar{\phi}(P) + \sum_{k=1}^{6} \phi_k(P;t) + \phi_I(P;t) + \phi_D(P;t) \tag{2.8}$$

where $\bar{\Phi}(P) + \bar{\phi}(P)$ denotes the velocity potential of the steady flow due to constant forward speed of the moving body. This is referred as the *steady* problem. The *radiation* problem is caused by a moving body with prescribed oscillatory motions of six degrees of freedom. With the kth mode of motion, for $k = 1, 2, \cdots, 6$, the respective radiated wave potential is denoted by ϕ_k. The potential of the incident waves is denoted by ϕ_I. In the *diffraction* problem, we denote ϕ_D or ϕ_7 as the potential of the diffracted waves. Note that in the steady-moving system, the fluid velocity in the far field will tend to be that of the uniform flow and the undisturbed incident wave.

2.3.1 The Neumann-Kelvin Linearization

The choice of a uniform flow alone, i.e., $\bar{\Phi} = -U_0 x$, leads to the Neumann-Kelvin approximation, where the pressure, the free-surface condition and the body boundary condition are given by:

$$p = -\rho(\phi_t - U_0\phi_x) \tag{2.9}$$

$$\left(\frac{\partial}{\partial t} - U_0\frac{\partial}{\partial x}\right)^2\phi + g\frac{\partial \phi}{\partial z} = 0, \quad \text{on } z = 0 \tag{2.10}$$

$$\frac{\partial(\phi_I + \phi_D)}{\partial n} = 0, \quad \text{on } \bar{S}_b \tag{2.11}$$

$$\frac{\partial \phi_k}{\partial n} = n_k\dot{x}_k + m_k x_k, \quad \text{on } \bar{S}_b \tag{2.12}$$

In equations (2.9) and (2.10), ϕ represents any of the perturbation potentials. $\bar{S}_b$ is the mean position of the floating body's surface, and n_k is the generalized unit normal defined as

$$\{n_k\} = (n_1, n_2, n_3, n_4, n_5, n_6) \tag{2.13}$$

where n_1, n_2 and n_3 are the components along the x-, y- and z-axis.

Let

$$\hat{\mathbf{n}} = (n_1, n_2, n_3) \tag{2.14}$$

and then

$$(n_4, n_5, n_6) = \mathbf{r_g} \times \hat{\mathbf{n}} \tag{2.15}$$

where $\mathbf{r}_g = (x - x_g, y - y_g, z - z_g)$ is the position vector from the center of gravity (x_g, y_g, z_g) of the floating body to a point $P(x, y, z)$ on the hull surface.

The steady and the unsteady potentials are coupled through the m-terms (Newman, 1978) in the body boundary conditions. In the Neumann-Kelvin linearization, the m-terms can be simplified to

$$m_k = (0, 0, 0, 0, U_0 n_3, -U_0 n_2) \tag{2.16}$$

2.3.2 The Double-Body Flow

The Neumann-Kelvin linearization works well for slender bodies. However, for more full-formed bodies, the approximation of the body boundary conditions are not satisfactory. As an alternative choice to improve the body-boundary condition, the double-body approximation includes a perturbation of the uniform stream. Then, the steady potential is

$$\Phi^{db} = -U_0 x + \phi^{db}, \tag{2.17}$$

which satisfies the following boundary-value problem,

$$\begin{aligned} &\nabla^2 \Phi^{db} = 0 \\ &\frac{\partial \Phi^{db}}{\partial z} = 0, \qquad \text{on } z = 0 \end{aligned} \tag{2.18}$$

$$\mathbf{n} \cdot \nabla\Phi^{db} = 0, \qquad \text{on } \bar{S}_b$$

$$\nabla\Phi^{db} \to (-U_0, 0, 0), \qquad \text{as } R_1 \to \infty$$

According to Newman (1978), the double-body m-terms can be written as

$$\begin{aligned}
(m_1, m_2, m_3) &= -(\mathbf{n} \cdot \nabla)\nabla\Phi^{db} \\
&= -(n_1\Phi^{db}_{xx} + n_2\Phi^{db}_{xy} + n_3\Phi^{db}_{xz},\ n_1\Phi^{db}_{yx} + n_2\Phi^{db}_{yy} + n_3\Phi^{db}_{yz}, \\
&\quad n_1\Phi^{db}_{zx} + n_2\Phi^{db}_{zy} + n_3\Phi^{db}_{zz})
\end{aligned} \tag{2.19}$$

$$\begin{aligned}
(m_4, m_5, m_6) &= \mathbf{r}_g \times (m_1, m_2, m_3) - \mathbf{n} \times \nabla\Phi^{db} \\
&= \mathbf{r}_g \times (m_1, m_2, m_3) + (n_3\Phi^{db}_y - n_2\Phi^{db}_z,\ n_1\Phi^{db}_z - n_3\Phi^{db}_x, \\
&\quad n_2\Phi^{db}_x - n_1\Phi^{db}_y)
\end{aligned} \tag{2.20}$$

where Φ^{db}_{xx}, Φ^{db}_{yy} and Φ^{db}_{zz} denote the second-order derivatives of the potential Φ^{db} about x, y and z, respectively; Φ^{db}_x, Φ^{db}_y and Φ^{db}_z are the velocities along x, y and z-directions; and Φ^{db}_{xy}, Φ^{db}_{xz}, Φ^{db}_{yx}, Φ^{db}_{yz}, Φ^{db}_{zx}, and Φ^{db}_{zy} are all the second-order cross derivatives of Φ^{db}.

In this thesis, the Neumann-Kelvin initial boundary value problem as stated in Section 2.3.1 is solved.

2.4 The Boundary Integral Equation

The radiation and diffraction perturbation problems mentioned above all satisfy the same boundary-value problem with different body boundary conditions. By using the time-dependent Green function and Green's theorem, the boundary integral equation can be obtained for the initial-boundary-value-problem discussed above. Details are given by Liapis (1986). The time-dependent Green function satisfies the free-surface, far field, radiation and diffraction conditions and initial conditions. It can be found in Wehausen and Laitone (1960, Eq. 13.49). By defining a field point, $P(x, y, z)$, and a source point, $Q(x', y', z')$, the time-dependent Green function for the infinite water depth can be written as:

$$G(P, Q; t-\tau) = G_0(P, Q)\delta(t-\tau) + H(t-\tau)F(P, Q; t-\tau) \tag{2.21}$$

with the Rankine source

$$G_0(P, Q) = -\frac{1}{4\pi}\left(\frac{1}{r} - \frac{1}{r_1}\right) \tag{2.22}$$

where $\delta(t-\tau)$ is the Dirac Delta function and $H(t-\tau)$ is the Heaviside unit step function, and

$$F(P, Q; t-\tau) = -\frac{1}{2\pi}\int_0^\infty \sqrt{gk}\sin[\sqrt{gk}(t-\tau)]e^{k(z+z')}J_0(kR)dk \tag{2.23}$$

with

$$r = \sqrt{(x-x')^2 + (y-y')^2 + (z-z')^2}, \tag{2.24}$$

$$r_1 = \sqrt{(x-x')^2 + (y-y')^2 + (z+z')^2}, \tag{2.25}$$

$$R = \sqrt{(x-x')^2 + (y-y')^2}, \tag{2.26}$$

and J_0 is the Bessel function of the zeroth order.

The Green function represents the potential at the field point P and at the time t due to an impulsive source at point Q suddenly created and destroyed completely at time $t = \tau$. The Green function is solved from the following equations:

$$\nabla^2 G(P,Q;t-\tau) = -4\pi\delta(P-Q)\delta(t-\tau) \tag{2.27}$$

$$(\frac{\partial}{\partial t} - U_0\frac{\partial}{\partial x})^2 G(P,Q;t-\tau) + g\frac{\partial G(P,Q;t-\tau)}{\partial z} = 0, \quad \text{on } z = 0 \tag{2.28}$$

$$G(P,Q;t-\tau), \frac{\partial G(P,Q;t-\tau)}{\partial t} = 0, \quad \text{for } t < 0 \tag{2.29}$$

Applying Green's theorem to the fluid domain Ω which is enclosed by $\bar{S}_b$, S_f, S_∞ and the bottom surface, leads to

$$\int_\Omega (\phi\nabla^2 G - G\nabla^2\phi)d\Omega = \int_{\bar{S}_b} (\phi\frac{\partial G}{\partial n} - G\frac{\partial\phi}{\partial n})dS \tag{2.30}$$

Integrating Eq.(2.30) with respect to τ from t_0 to t, applying the properties of $G(P,Q;t-\tau)$ and considering the free surface contribution yields

$$
\begin{aligned}
\phi(P,t) &= \int_{t_0}^{t} d\tau \int_{\bar{S}_b} \left[\phi(Q;\tau) \frac{\partial G(P,Q;t-\tau)}{\partial n_Q} - G(P,Q;t-\tau) \frac{\partial \phi(Q;\tau)}{\partial n_Q} \right] dS \\
&- \frac{1}{g} \int_{t_0}^{t} d\tau \oint_{\Gamma} U_0^2 \left[G(P,Q;t-\tau) \frac{\partial \phi(Q;\tau)}{\partial x'} - \phi(Q;\tau) \frac{\partial G(P,Q;t-\tau)}{\partial x'} \right] dl \\
&+ \frac{1}{g} \int_{t_0}^{t} d\tau \oint_{\Gamma} U_0 \left[G(P,Q;t-\tau) \frac{\partial \phi(Q;\tau)}{\partial \tau} - \phi(Q;\tau) \frac{\partial G(P,Q;t-\tau)}{\partial \tau} \right] dl
\end{aligned}
\tag{2.31}
$$

The above integral equation gives the velocity potential at any point $P(x, y, z)$ in the fluid Ω. Details were given by Liapis (1986). In Eq.(2.31), t_0 represents the initial time which is zero for the radiation problem and $-\infty$ for the diffraction problem; and Γ is the intersection of the hull surface and the calm water plane $z = 0$. The positive line integral is in the counter-clockwise direction.

Considering an interior flow and subtracting it from Eq.(2.31), the final integral equation in terms of source strength distribution can be obtained as:

$$
\begin{aligned}
\phi(P,t) &= \int_{t_0}^{t} d\tau \int_{\bar{S}_b} G(P,Q;t-\tau)\sigma(Q;\tau) dS \\
&+ \frac{U_0^2}{g} \int_{t_0}^{t} d\tau \oint_{\Gamma} n_1 G(P,Q;t-\tau)\sigma(Q;\tau) dl
\end{aligned}
\tag{2.32}
$$

where σ is the source strength which can be solved from

$$\frac{\partial \phi(P;t)}{\partial n_P} = -\frac{1}{2}\sigma(P;t) + \int_{t_0}^{t} d\tau \int_{\bar{S}_b} \frac{\partial G(P,Q;t-\tau)}{\partial n_P}\sigma(Q;\tau)dS + \frac{U_0^2}{g}\int_{t_0}^{t} d\tau \oint_{\Gamma} \left[n_1 \frac{\partial G(P,Q;t-\tau)}{\partial n_P}\sigma(Q;\tau)\right] dl \tag{2.33}$$

where n_1 is the x-component of the unit normal vector.

2.4.1 Computation of Forces

The forces caused by the radiated and diffracted waves can be obtained by the integration of pressure. The force acting on the body surface in any of the six modes of motion, say the jth mode, is given by

$$F_j(t) = \int_{\bar{S}_b} p(P;t) n_j dS \tag{2.34}$$

where $p(P;t)$ is the linearized pressure defined in Eq.(2.9), which is equivalent to

$$p(P;t) = -\rho\frac{\partial \phi}{\partial t} - \rho \mathbf{W}\cdot\nabla\phi \tag{2.35}$$

where $\mathbf{W} = (-U_0, 0, 0)$. The force can be rewritten as

$$F_j(t) = -\rho\int_{\bar{S}_b}\left[\frac{\partial \phi}{\partial t} + \mathbf{W}\cdot\nabla\phi\right] n_j dS \tag{2.36}$$

Employing the theorem derived by Ogilvie and Tuck (1969)

$$\int_{\bar{S}_b} [m_j \phi + n_j (\mathbf{W} \cdot \nabla \phi)] dS = - \oint_{\Gamma} \phi n_j (\mathbf{l} \times \mathbf{n}) \cdot \mathbf{W} dl \tag{2.37}$$

and applying to Eq.(2.36) yields

$$F_j(t) = -\rho \int_{\bar{S}_b} \frac{\partial \phi}{\partial t} n_j dS + \rho \int_{\bar{S}_b} \phi m_j dS + \rho \oint_{\Gamma} \phi n_j (\mathbf{l} \times \mathbf{n}) \cdot \mathbf{W} dl \tag{2.38}$$

where $\mathbf{l}$ is the line vector along the waterline. Introducing

$$g_{jk}(t) = \rho \int_{\bar{S}_b} \phi_k(t) n_j dS \tag{2.39}$$

$$h_{jk}(t) = -\rho \int_{\bar{S}_b} \phi_k(t) m_j dS - \rho \oint_{\Gamma} \phi_k(t) n_j (\mathbf{l} \times \mathbf{n}) \cdot \mathbf{W} dl \tag{2.40}$$

where k is from 1 to 6 for the radiation problem and 7 for the diffraction problem, the force due to the excitation in the kth mode of motion can then be written as

$$F_{jk}(t) = -\dot{g}_{jk}(t) - h_{jk}(t) \tag{2.41}$$

where $\dot{g}_{jk}(t) = \partial g_{jk}(t)/\partial t$.

2.5 Solving the Radiation Problem with the Impulse Response Function

In this section, the radiation problem and its solution through the usage of the impulse response function method will be described. The initial-boundary-value-problem can be solved in terms of the radiation potential functions, $\phi_k(x, y, z; t)$, for $k = 1, 2, ...6$, which satisfy the Laplace equation subject to the linear free-surface conditions, the body boundary conditions, the far field conditions and the initial conditions as follows:

$$\begin{aligned}
\nabla^2\phi_k &= 0, && \text{in} \quad \Omega \\
(\frac{\partial}{\partial t} - U_0\frac{\partial}{\partial z})^2\phi_k + g\frac{\partial\phi_k}{\partial z} &= 0, && \text{on} \quad z = 0 \\
\frac{\partial\phi_k}{\partial n} &= n_k\dot{x}_k + m_k x_k, && \text{on} \quad \bar{S}_b \\
\nabla\phi_k &\to 0, && \text{as} \quad R_1 \to \infty, \quad \text{on } z = 0 \\
\nabla\phi_k &\to 0, && \text{as} \quad z \to -\infty \\
\phi_k = 0, \ \frac{\partial\phi_k}{\partial t} &= 0, && \text{at} \quad t = 0
\end{aligned} \tag{2.42}$$

where x_k denotes the motion displacement in the kth direction. If the initial-boundary-value-problem for radiation is linearized, then the radiation problem can be decomposed by introducing the impulse response function as described by Liapis (1986) as follows:

According to the method proposed by Cummins (1962) and later elaborated by

Ogilvie (1964). we consider that the body is given an impulsive motion at $t = 0$ in the kth mode with a velocity $\dot{\xi}_k(t) = \delta(t)$, then the body boundary condition becomes

$$\frac{\partial \phi_k}{\partial n} = n_k \delta(t) + m_k H(t), \quad \text{for } k = 1, 2, \cdots, 6 \tag{2.43}$$

The body boundary condition (2.43) suggests that the potential ϕ_k can be decomposed into an impulsive part and a memory part as

$$\phi_k(P;t) = \psi_k(P)\delta(t) + \chi_k(P)H(t) \tag{2.44}$$

where both ψ_k and χ_k satisfy the body boundary condition (2.43) for all time if we set

$$\begin{aligned} \frac{\partial \psi_k}{\partial n} &= n_k, \quad \text{on } \bar{S}_b \\ \frac{\partial \chi_k}{\partial n} &= m_k, \quad \text{on } \bar{S}_b \end{aligned} \tag{2.45}$$

The ψ_k potential describes the fluid motion during the impulsive stage and satisfies

$$\begin{aligned} \psi_k &= 0, & &\text{on} \quad z = 0 \\ \frac{\partial \psi_k}{\partial n} &= n_k, & &\text{on} \quad \bar{S}_b \\ \nabla \psi_k &\to 0, & &\text{at} \quad S_\infty \end{aligned} \tag{2.46}$$

The χ_k potential represents the motion of the fluid subject to an initial impulse and is composed of two components. The first component is due to the change of body orientation caused by the impulse in velocity. After the impulse in velocity the body will have a unit displacement in the kth mode. It results in a change of fluid velocity on the body surface. Since the body is in the steady flow field, in order to satisfy the body boundary condition, this change must be subdued. Therefore, $\partial\chi_k/\partial n$ must have the value m_k on the body surface for all $t \geq 0$. The second component is the result of the impulsive velocity inducing a disturbance into the flow field which will propagate as a wave motion away from the body at subsequent times. Therefore, χ_k will satisfy the free surface condition for $t > 0$ and the initial condition,

$$\begin{aligned} \chi_k &= 0, & &\text{on} \quad z = 0 \\ \frac{\partial \chi_k}{\partial t} &= -g\frac{\partial \psi_k}{\partial z}, & &\text{on} \quad z = 0 \end{aligned} \tag{2.47}$$

Considering these two components, χ_k can be written as

$$\chi_k = \varphi_k H(t) + \bar{\chi}_k \tag{2.48}$$

where φ_k represents the potential caused by the unit displacement during the impulsive stage of the motion. It satisfies the following boundary conditions:

$$\begin{aligned} \frac{\partial \varphi_k}{\partial n} &= m_k, &\quad \text{on} \quad & \bar{S}_b \\ \varphi_k &= 0, &\quad \text{on} \quad & z = 0 \\ \nabla \varphi_k &\to 0, &\quad \text{at} \quad & S_\infty \end{aligned} \tag{2.49}$$

The potential of the second component $\bar{\chi}_k$ satisfies the following conditions:

$$\begin{aligned} \bar{\chi}_k &= 0, &\quad \text{at} \quad & t = 0 \\ \frac{\partial \bar{\chi}_k}{\partial t} &= -g\frac{\partial \psi_k}{\partial z}, &\quad \text{on} \quad & z = 0 \ \text{ at } t = 0 \\ \frac{\partial^2 \bar{\chi}_k}{\partial t^2} &= -g\frac{\partial \varphi_k}{\partial z}, &\quad \text{on} \quad & z = 0 \ \text{ at } t = 0 \\ \frac{\partial \bar{\chi}_k}{\partial n} &= 0, &\quad \text{on} \quad & \bar{S}_b \ \text{ for } t \geq 0 \\ \left[(\frac{\partial}{\partial t} - U_0\frac{\partial}{\partial x})^2 + g\frac{\partial}{\partial z} \right] (\bar{\chi}_k + \varphi_k) &= 0, &\quad \text{on} \quad & z = 0 \ \text{ for } t \geq 0 \end{aligned} \tag{2.50}$$

Using Eq.(2.48), the potential for an arbitrary forced motion in terms of a velocity,

$\dot{\xi}_k(t)$, for the kth mode of motion, can be found by integrating Eq.(2.44) as follows:

$$\begin{aligned} \phi_k(P;t) &= \int_0^t \phi_k(P;\tau)\dot{\xi}_k(t-\tau)d\tau \\ &= \psi_k(P)\dot{\xi}_k(t) + \varphi_k(P)\xi_k(t) + \int_0^t \bar{\chi}_k(P;\tau)\dot{\xi}_k(t-\tau)d\tau \end{aligned} \tag{2.51}$$

where $\phi_k(P;t)$ satisfies the body boundary condition, the free surface condition, and the conditions at infinity for all times (Cummins, 1962). Note that ψ_k, φ_k and $\bar{\chi}_k$ can be solved from Eq.(2.46), Eq.(2.49) and Eq.(2.50), respectively.

Substituting Eq(2.51) into Eq.(2.38), the radiation force can be expressed as:

$$F_{jk}(t) = -\bar{\mu}_{jk}\ddot{\xi}_k(t) - \bar{\lambda}_{jk}\dot{\xi}_k(t) - \bar{\gamma}_{jk}\xi_k(t) - \int_0^t K_{jk}^R(t-\tau)\dot{\xi}_k(\tau)d\tau \tag{2.52}$$

where

$$\begin{aligned} \bar{\mu}_{jk} &= \rho\int_{\bar{S}_b} \psi_k n_j dS \\ \bar{\lambda}_{jk} &= \rho\int_{\bar{S}_b} \varphi_k n_j dS - \rho\int_{\bar{S}_b} \psi_k m_j dS \\ &\quad -\rho\oint_{\Gamma} \psi_k n_j(\mathbf{l}\times\mathbf{n})\cdot\mathbf{W}dl \\ \bar{\gamma}_{jk} &= -\rho\int_{\bar{S}_b} \varphi_k m_j dS - \rho\oint_{\Gamma} \varphi_k n_j(\mathbf{l}\times\mathbf{n})\cdot\mathbf{W}dl \\ K_{jk}^R(t) &= \rho\int_{\bar{S}_b} \frac{\partial\bar{\chi}_k}{\partial t} n_j dS - \rho\int_{\bar{S}_b} \bar{\chi}_k m_j dS \\ &\quad -\rho\oint_{\Gamma} \bar{\chi}_k n_j(\mathbf{l}\times\mathbf{n})\cdot\mathbf{W}dl \end{aligned}$$

where $\bar{\mu}_{jk}$ is the added-mass of the floating body in the time domain which depends on the body geometry; $\bar{\lambda}_{jk}$ is the hydrodynamic damping coefficient depending on the body geometry and the forward speed; $\bar{\gamma}_{jk}$ is the coefficient of the hydrodynamic restoring force in the time domain, which also depends on the body geometry and the forward speed; and $K_{jk}^R(t)$ is a function of the body geometry, speed and time and shows the memory effect of the impulse motion.

The impulse response function, K_{jk}^R, can be obtained by using a non-impulsive input velocity:

$$\dot{\xi}_k(t) = \sqrt{\frac{\alpha}{\pi}} e^{-\alpha t^2} \tag{2.53}$$

The use of a non-impulsive input can eliminate the high frequency content of input, thus avoiding numerical problems. Here, α is an arbitrary constant which controls the frequency content of the input. It is easily shown that as $\alpha \to \infty$ the input is identical to $\dot{\xi}_k = \delta(t)$. The input velocity has the following properties:

$$\xi_k(t) = \frac{1}{2}\left[1 + \mathrm{erf}(\sqrt{\alpha}t)\right] \tag{2.54}$$

and

$$\ddot{\xi}_k(t) = -2\alpha t \dot{\xi}_k(t) \tag{2.55}$$

Under this non-impulsive input, the body boundary condition becomes,

$$\frac{\partial \phi_k}{\partial n} = n_k \dot{\xi}_k(t) + m_k \xi_k(t) \tag{2.56}$$

Comparing Eq.(2.41) and Eq.(2.52), the radiation problem leads to

$$\int_0^t K_{jk}^R(t-\tau)\dot{\xi}_k(\tau)d\tau = \dot{g}_{jk}(t) + h_{jk}(t) - \bar{\mu}_{jk}\ddot{\xi}_k(t) - \bar{\lambda}_{jk}\dot{\xi}_k(t) - \bar{\gamma}_{jk}\xi_k(t) \tag{2.57}$$

Then the impulse response function, K_{jk}^R, can be solved for a short duration based on the non-impulsive input $\dot{\xi}_k(t)$ from Eq.(2.57). The numerical solution of the impulse response function is given in Appendix A.

The radiation force acting on a floating body with arbitrary motion $x_k(t)$ can be computed with the following equation:

$$F_{jk}(t) = -\bar{\mu}_{jk}\ddot{x}_k(t) - \bar{\lambda}_{jk}\dot{x}_k(t) - \bar{\gamma}_{jk}x_k(t) - \int_0^t K_{jk}^R(t-\tau)\dot{x}_k(\tau)d\tau \tag{2.58}$$

2.6 Solving the Diffraction Problem with the Impulse Response Function

The diffracted wave potential, $\phi_7(P;t)$, satisfies the Laplace equation subject to the boundary conditions, the far field conditions and the initial conditions as follows:

$$\begin{aligned}
\nabla^2\phi_7 &= 0 && \text{in} \quad \Omega \\
(\frac{\partial}{\partial t} - U_0\frac{\partial}{\partial z})^2\phi_7 + g\frac{\partial\phi_7}{\partial z} &= 0, && \text{on} \quad z=0 \\
\frac{\partial\phi_7}{\partial n} &= -\frac{\partial\phi_I}{\partial n}, && \text{on} \quad \bar{S}_b \\
\nabla\phi_7 &\to 0, && \text{as} \quad R_1 \to \infty, \text{ on } z=0 \\
\nabla\phi_7 &\to 0, && \text{as} \quad z \to -\infty \\
\phi_7 = 0, \ \frac{\partial\phi_7}{\partial t} &= 0, && \text{as} \quad t \to -\infty
\end{aligned} \tag{2.59}$$

As with the radiation problem, we can use a non-impulsive incident wave to determine the diffracted wave force. For the case of a moving body with a forward speed, a non-impulsive incident wave at the origin of the steady-moving coordinate system can be chosen as,

$$\bar{\eta}_0(t) = \frac{1}{\pi}\mathrm{Re}\left(\int_0^\infty e^{-\omega^2/4\alpha}e^{i\omega_e t}d\omega_e\right) \tag{2.60}$$

where α is an arbitrary constant. which can be set as the same value as used in the radiation problem; $\omega_e = \omega - U_0\omega^2/g\cos\beta$ is the frequency of encounter; β is the heading angle of wave propagation relative to the x-axis, where 180^0 denotes head seas; and ω is the wave frequency. Corresponding to the non-impulsive wave elevation, the derivatives of the incident wave potential can be obtained as:

$$\nabla\bar{\phi}_0(x, y, z; t) = \frac{1}{\pi}\mathrm{Re}\left(\left\{\begin{array}{c}\cos\beta \\ \sin\beta \\ i\end{array}\right\}\int_0^\infty \omega e^{k(z-i\varpi)} e^{-\omega^2/4\alpha} e^{i\omega_e t} d\omega_e\right) \tag{2.61}$$

where $\varpi = x\cos\beta + y\sin\beta$, $k = \omega^2/g$, the wave number and Re() denotes the real part of the complex function. The details on the original derivation of $\bar{\eta}_0$ and $\nabla\bar{\phi}_0$ were given by King (1987) and King *et al.* (1988).

With the non-impulsive incident wave $\bar{\eta}_0$, the body boundary condition in Eq.(2.59) becomes

$$\frac{\partial\phi_7}{\partial n} = -\frac{\partial\bar{\phi}_0}{\partial n} \tag{2.62}$$

The impulse response function $K_{j7}^D(t)$ can be solved from the following equation:

$$\int_{-\infty}^{\infty} K_{j7}^D(t-\tau)\bar{\eta}_0(\tau)d\tau = -\dot{g}_{j7}(t) - h_{j7}(t) \tag{2.63}$$

where

$$g_{j7}(t) = \rho\int_{\bar{S}_b} \phi_7(t) n_j dS \tag{2.64}$$

$$h_{j7}(t) = -\rho\int_{\bar{S}_b} \phi_7(t) m_j dS - \rho\oint_\Gamma \phi_7(t) n_j (\mathbf{l}\times\mathbf{n})\cdot\mathbf{W} dl \tag{2.65}$$

The diffraction force due to incident waves η_0 can be computed as

$$F_{j7}(t) = \int_{-\infty}^{\infty} K_{j7}^{D}(t - \tau)\eta_0(\tau)d\tau \tag{2.66}$$

Chapter 3

The Panel-Free Method

3.1 Desingularization of the Boundary Integral Equation

The singularity of the boundary integral equation is contained in the Rankine source term of the time-dependent Green function. For a floating body, if the waterline integral is omitted for its relatively small contribution to integration for wall-sized bodies, Eq.(2.33) can be written as

$$V_n(P;t) = \frac{\partial \phi(P;t)}{\partial n_P} = -\frac{1}{2}\sigma(P;t) + \int_{t_0}^{t} d\tau \int_{\bar{S}_b} \frac{\partial G(P,Q;t-\tau)}{\partial n_P} \sigma(Q;\tau) dS \qquad (3.1)$$

where P is the field point and Q is the source point.

Substituting the Green function $G(P,Q;t-\tau)$ as in Eq.(2.21) into Eq.(3.1) yields

$$\begin{aligned} V_n(P;t) = &-\frac{1}{2}\sigma(P;t) + \int_{\bar{S}_b} \sigma(Q;t)\frac{\partial G_0(P,Q)}{\partial n_P}dS \\ &+ \int_{t_0}^{t} d\tau \int_{\bar{S}_b} \frac{\partial F(P,Q;t-\tau)}{\partial n_P}\sigma(Q;\tau)dS \end{aligned} \tag{3.2}$$

Based on Gauss's flux theorem

$$\int_{\bar{S}_b+\bar{S}_b'} \frac{\partial}{\partial n_Q}\left(\frac{1}{r}\right) dS_Q = 2\pi \tag{3.3}$$

where $\mathbf{n}_Q$ is the normal vector pointing into the body surface and we can write

$$\int_{\bar{S}_b+\bar{S}_b'} \sigma(Q)\frac{\partial}{\partial n_P}(\frac{1}{r})dS_Q = \int_{\bar{S}_b+\bar{S}_b'} \left[\sigma(Q)\frac{\partial}{\partial n_P}(\frac{1}{r}) - \sigma(P)\frac{\partial}{\partial n_Q}(\frac{1}{r})\right] dS_Q + 2\pi\sigma(P) \tag{3.4}$$

where $\bar{S}_b'$ denotes the image of $\bar{S}_b$. By using the Taylor expansion to the third order, Landweber and Macagno (1969) have shown the integral term in the right-hand-side (RHS) of Eq.(3.4) is zero when P coincides with Q. Therefore, the singularity of $1/r$ can be removed by applying Eq.(3.4). Equation (3.4) is, in fact, equivalent to

$$\int_{\bar{S}_b} \sigma(Q)\frac{\partial}{\partial n_P}(\frac{1}{r}+\frac{1}{r_1})dS_Q = 2\pi\sigma(P) + \int_{\bar{S}_b}\left[\sigma(Q)\frac{\partial}{\partial n_P}(\frac{1}{r}+\frac{1}{r_1}) - \sigma(P)\frac{\partial}{\partial n_Q}(\frac{1}{r}+\frac{1}{r_1})\right]dS_Q \quad (3.5)$$

Defining

$$G_1(P,Q) = -\frac{1}{4\pi}(\frac{1}{r}+\frac{1}{r_1}) \quad (3.6)$$

$$G_2(P,Q) = \frac{1}{4\pi}\frac{1}{r_1} \quad (3.7)$$

the Rankine source term of the Green function can be written as

$$G_0(P,Q) = G_1(P,Q) + 2G_2(P,Q) \quad (3.8)$$

Substituting Eq.(3.8) into Eq.(3.2) yields

$$V_n(P;t) = -\frac{1}{2}\sigma(P;t) + \int_{\bar{S}_b}\sigma(Q;t)\frac{\partial G_1(P,Q)}{\partial n_P}dS + 2\int_{\bar{S}_b}\sigma(Q;t)\frac{\partial G_2(P,Q)}{\partial n_P}dS + \int_{t_0}^{t}d\tau\int_{\bar{S}_b}\frac{\partial F(P,Q;t-\tau)}{\partial n_P}\sigma(Q;\tau)dS \quad (3.9)$$

Based on Eq.(3.5) and Eq.(3.9), Eq.(3.2) can be desingularized as

$$V_n(P;t) = -\sigma(P;t) + \int_{\bar{S}_b} \left[\sigma(Q;t)\frac{\partial G_1(P,Q)}{\partial n_P} - \sigma(P;t)\frac{\partial G_1(P,Q)}{\partial n_Q} \right] dS \tag{3.10}$$
$$+2\int_{\bar{S}_b} \sigma(Q;t)\frac{\partial G_2(P,Q)}{\partial n_P} dS + \int_{t_0}^{t} d\tau \int_{\bar{S}_b} \frac{\partial F(P,Q;t-\tau)}{\partial n_P}\sigma(Q;\tau)dS$$

As shown in Eq.(3.10), the second term in RHS is zero as $P \rightarrow Q$ and all other terms are regular. Here, $V_n(P;t)$ is given by $-\partial\phi(P;t)/\partial n_P$ for the radiation problem and $-\partial\phi_I(P;t)/\partial n_P$ for the diffraction problem. After the source strength, σ, is solved from Eq.(3.10), the velocity potential then can be obtained from Eq.(2.33). Omitting the line integral, Eq.(2.33) can be written as follows:

$$\begin{aligned} \phi(P,t) &= \int_{t_0}^{t} d\tau \int_{\bar{S}_b} G_1(P,Q;t-\tau)\sigma(Q;\tau)dS \\ &+ 2\int_{\bar{S}_b} \sigma(Q;t)G_2(P,Q)dS + \int_{t_0}^{t} d\tau \int_{\bar{S}_b} F(P,Q;t-\tau)\sigma(Q;\tau)dS \end{aligned} \tag{3.11}$$

The singularity appears only in the first term in RHS and it can be removed based on the procedure proposed by Landweber and Macagno (1969). Introducing a source strength distribution $\gamma(P)$ on $\bar{S}_b$ which makes the body surface an equipotential surface, then the integral equation for the velocity potential can be desingularized as follows:

$$\phi(P;t) = \int_{\bar{S}_b} G_1(P,Q)\left[\sigma(Q;t) - \gamma(Q)\frac{\sigma(P;t)}{\gamma(P)}\right] dS + \phi_0\frac{\sigma(P;t)}{\gamma(P)} \tag{3.12}$$
$$+2\int_{\bar{S}_b} \sigma(Q;t)G_2(P,Q)dS + \int_{t_0}^{t} d\tau \int_{\bar{S}_b} \sigma(Q;\tau)F(P,Q;t-\tau)dS$$

It can be seen from the first term in RHS of Eq.(3.12) that the singular term is zero when P coincides with Q. Here $\gamma(P)$ makes the body surface as an equipotential surface of potential ϕ_0 and satisfies the homogeneous integral equation

$$\gamma(P) = -\int_{\bar{S}_b} \gamma(Q)\frac{\partial K(P,Q)}{\partial n_P}dS \tag{3.13}$$

Eq.(3.13) can be desingularized in a similar way to Eq.(3.10), and $\gamma(P)$ can be solved iteratively by finding the eigenfunction of $\partial K(P,Q)/\partial n_P$ associated with the eigenvalue equal to -1, where $K(P,Q) = 2G_1(P,Q)$. Since the potential, ϕ_0, is constant in the interior of the equipotential surface, its value can be computed at the origin by

$$\phi_0 = -\frac{1}{4\pi}\int_{\bar{S}_b} \gamma(Q)\left(\frac{1}{|Q|} + \frac{1}{|Q'|}\right)dS \tag{3.14}$$

where $|Q|$ and $|Q'|$ denote distances between Q and the origin, and Q', the image of Q, and the origin, respectively.

3.2 NURBS Representation of the Body Geometry

While many mathematical representations have been adopted to describe the body surface, for example, cubic polynomials and conformal mapping, non-uniform rational B-Splines (NURBS) (Piegl and Tiller, 1987, Farin, 1991) have become the preferred method. The widespread acceptance and popularity of NURBS are because they provide a general and flexible description for a large class of free-form geometric shape. Their intrinsic characteristics of local control, low memory requirement, coupled with a stable and efficient generating algorithm, make them a powerful geometric tool for surface description, especially for complicated body geometry. In this work, NURBS were adopted to describe the body surface mathematically. A brief introduction of NURBS is given in Appendix B.

It is assumed that there are N_p patches or parts to describe a body surface. Each patch can be represented by a NURBS surface. Let $P(x(u,v), y(u,v), z(u,v))$ be a point on a patch, where x, y and z denote the Cartesian coordinate components, and u and v are two parameters for the surface definition. Applying the NURBS surface, $P(u,v)$ can be defined as follows:

$$P(u,v) = \frac{\sum_{i=0}^{n}\sum_{j=0}^{m} w_{ij} C_{i,j} N_{i,p}(u) N_{j,q}(v)}{\sum_{i=0}^{n}\sum_{j=0}^{m} w_{ij} N_{i,p}(u) N_{j,q}(v)} \tag{3.15}$$

where n and m are the number of control points along u and v directions, respectively; w_{ij} are the weights; $C_{i,j}$ form a network of control points; and $N_{i,p}(u)$ and $N_{j,q}(v)$ are the normalized B-splines basis functions of degrees p and q in the u and v directions, respectively.

The basis functions can be defined recursively as

$$N_{i,0}(u) = \begin{cases} 1 & \text{if } u_i \leq u < u_{i+1} \\ 0 & \text{otherwise} \end{cases} \tag{3.16}$$

$$N_{i,p}(u) = \frac{u - u_i}{u_{i+p} - u_i} N_{i,p-1}(u) + \frac{u_{i+p+1} - u}{u_{i+p+1} - u_{i+1}} N_{i+1,p-1}(u) \tag{3.17}$$

where u_i defines the knot vector as

$$\mathbf{U} = \{0, 0, ..., 0, u_{p+1}, ..., u_{r-p-1}, 1, 1, ..., 1\} \tag{3.18}$$

In the v direction, v_i forms a knot vector as

$$\mathbf{V} = \{0, 0, ..., 0, v_{q+1}, ..., v_{s-q-1}, 1, 1, ..., 1\} \tag{3.19}$$

where the end knots are repeated with multiplicities $p + 1$ and $q + 1$, respectively, and $r = n + p + 1$ and $s = m + q + 1$.

The normal vector at $\mathbf{P}(u, v)$ is given by

$$\mathbf{N}_p = \frac{\partial \mathbf{P}(u,v)}{\partial u} \times \frac{\partial \mathbf{P}(u,v)}{\partial v} = (g_1, g_2, g_3) \tag{3.20}$$

where

$$g_1 = \frac{\partial y}{\partial u}\frac{\partial z}{\partial v} - \frac{\partial y}{\partial v}\frac{\partial z}{\partial u} \tag{3.21}$$

$$g_2 = \frac{\partial z}{\partial u}\frac{\partial x}{\partial v} - \frac{\partial z}{\partial v}\frac{\partial x}{\partial u} \tag{3.22}$$

$$g_3 = \frac{\partial x}{\partial u}\frac{\partial y}{\partial v} - \frac{\partial x}{\partial v}\frac{\partial y}{\partial u} \tag{3.23}$$

The differential of area is then given by

$$dS(u,v) = |\frac{\partial \mathbf{P}}{\partial u} \times \frac{\partial \mathbf{P}}{\partial v}|dudv = |J|dudv \tag{3.24}$$

where the Jacobian of $\mathbf{P}(u,v)$ is given as

$$|J| = (g_1^2 + g_2^2 + g_3^2)^{1/2} \tag{3.25}$$

Then the unit normal vector can be obtained from

$$\mathbf{n} = \mathbf{N}_P/|J| \tag{3.26}$$

3.3 Numerical Implementation of the Desingularized Integral Equation

Since Eq.(3.10) is singularity free, it can be discretized by directly applying the Gaussian quadrature. Introducing a computational space rs which is from -1 to 1, the Gaussian quadrature points are then arranged in the rs space. The mapping relationship of the computational space rs, the parametric space uv and the physical space xyz is illustrated in Figure 3.1.

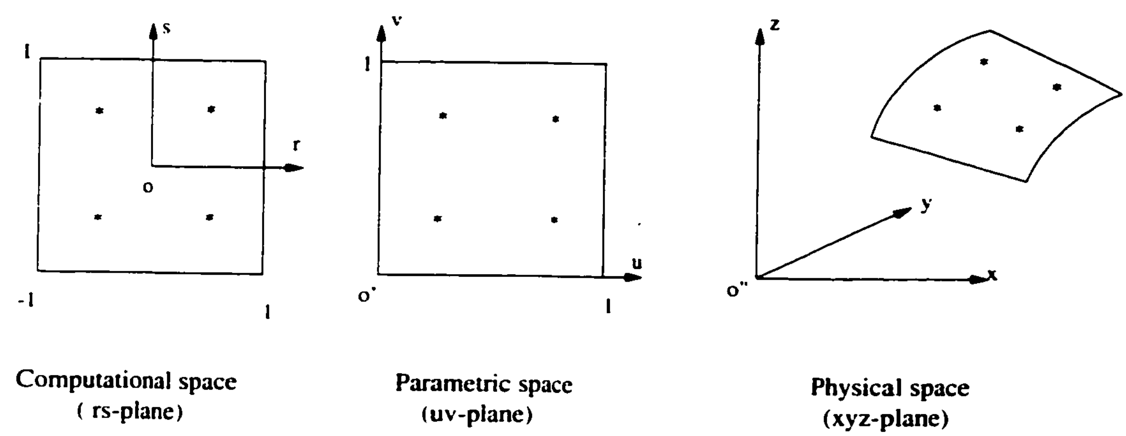

Figure 3.1: Mapping relationship for the computational space, the parametric space and the physical space

Coordinates, Jacobian and normals in the physical space corresponding to the Gaussian quadrature points can be obtained from Eq.(3.15), Eq.(3.25) and Eq.(3.26).

By applying the trapezoidal time integration scheme, Eq.(3.10) can be written as

$$V_n(P_i;t) = -\sigma(P_i;t) + \sum_{j=1}^{N_p}\sum_{r=1}^{N_j}\sum_{s=1}^{M_j} w_r w_s[\sigma(Q_j^{rs};t)\nabla_P G_1(P_i,Q_j^{rs})\cdot \mathbf{n}_{p_i} - \sigma(P_i;t)\nabla_Q G_1(P_i,Q_j^{rs})\cdot \mathbf{n}_{q_j^{rs}}]J_j^{rs}$$
$$+2\sum_{j=1}^{N_p}\sum_{r=1}^{N_j}\sum_{s=1}^{M_j} w_r w_s \sigma(Q_j^{rs};t)\nabla_P G_2(P_i,Q_j^{rs})\cdot \mathbf{n}_{p_i} J_j^{rs}$$
$$+\frac{1}{2}\Delta t\sum_{j=1}^{N_p}\sum_{r=1}^{N_j}\sum_{s=1}^{M_j} w_r w_s \sigma(Q_j^{rs};t_0)\frac{\partial F(P_i,Q_j^{rs};t)}{\partial n_P}J_j^{rs}+$$
$$\Delta t\sum_{k=1}^{k_t-1}\sum_{j=1}^{N_p}\sum_{r=1}^{N_j}\sum_{s=1}^{M_j} w_r w_s \frac{\partial F(P_i,Q_j^{rs};t-t_k)}{\partial n_P}\sigma(Q_j^{rs};t_k)J_j^{rs}, \quad \text{for} \quad i=1,2,...,N_p \tag{3.27}$$

where N_j and M_j are the number of Gaussian quadrature points in the u- and v-directions on the jth patch. $P_i = P_i(u_n, v_m), n = 1, ...N_i, m = 1, ...M_i$ and $Q_j^{rs} = Q_j(u_r, v_s)$, r=1,2,...,N_j, s=1,2,...,M_j, are the position vectors of Gaussian quadrature points on the ith and jth patches in the physical space, respectively; $\mathbf{n}_{p_i}$ and $\mathbf{n}_{q_j^{rs}}$ are the corresponding unit normals; w_r and w_s are the weighting coefficients in the u- and v-directions; J_j^{rs} is the Jacobian of Q_j^{rs}; t is the time; Δt is the time step; t_0 is the starting time, which is zero for the radiation problem and $-N_t\Delta t/2$ for the diffraction problem, where N_t is the number of total time steps; $t_k = k\Delta t$ and $t = k_t\Delta t$, where k and k_t are the time constants at any instant and for the total time, respectively. It can be seen that the algorithm is controlled by the number and arrangement of Gaussian quadrature points along u- and v-directions.

Introducing $W_J = w_r w_s J_j^{rs}$, $N = \sum_{j=1}^{N_p} N_j M_j$, $G_{1_{IJ}} = G_1(P_i, Q_j^{rs})$, and $G_{2_{IJ}} = G_2(P_i, Q_j^{rs})$, the above linear equation can be simplified as

$$\sum_{J=1}^{N} A_{IJ}\sigma_J = B_I, \quad I = 1, ..., N \tag{3.28}$$

with

$$A_{II} = -1 - \sum_{J=1,J\neq I}^{N} W_J \nabla G_{1_{IJ}} \cdot \mathbf{n}_J + 2W_I \nabla G_{2_{II}} \cdot \mathbf{n}_I \tag{3.29}$$

$$A_{IJ} = W_J \nabla G_{1_{IJ}} \cdot \mathbf{n}_I + 2W_J \nabla G_{2_{IJ}} \cdot \mathbf{n}_I, \ I \neq J \tag{3.30}$$

$$B_I = V_{n_I}^{k_t} - \Delta t \left[\frac{1}{2} \sum_{J=1}^{N} W_J \sigma_J^0 F_{n_{IJ}}^{k_t} + \sum_{k=1}^{k_t-1} \sum_{J=1}^{N} W_J F_{n_{IJ}}^{k_t-k} \sigma_J^k \right] \tag{3.31}$$

where

$$V_{n_I}^{k_t} = V_n(P_i; t) \tag{3.32}$$

$$\sigma_J^0 = \sigma(Q_j^{rs}; 0) \tag{3.33}$$

$$\sigma_J^k = \sigma(Q_j^{rs}; t_k) \tag{3.34}$$

$$F_{n_{IJ}}^{k_t} = \frac{\partial F(P_i, Q_j^{rs}; t)}{\partial n_P} \tag{3.35}$$

$$F_{n_{IJ}}^{k_t-k} = \frac{\partial F(P_i, Q_j^{rs}; t - t_k)}{\partial n_P} \tag{3.36}$$

Introducing $F_{IJ}^{k_t-k} = F(P_i, Q_j^{rs}; t - t_k)$, $F_{IJ}^{k_t} = F(P_i, Q_j^{rs}; t)$, $\gamma_I = \gamma(P_i)$ and $\gamma_J = \gamma(Q_j^{rs})$, the velocity potential, $\phi_I^{k_t}$, at time t on the body surface is obtained by the following equation,

$$\phi_I^{k_t} = \sum_{J=1}^{N} W_J G_{1_{IJ}} (\sigma_J^{k_t} - \gamma_J \frac{\sigma_I^{k_t}}{\gamma_I}) + 2 \sum_{J=1}^{N} W_J \sigma_J^{k_t} G_{2_{IJ}} + \phi_0 \frac{\sigma_I^{k_t}}{\gamma_I}$$
$$+ \left[\sum_{k=1}^{k_t-1} \sum_{J=1}^{N} W_J \sigma_J^k F_{IJ}^{k_t-k} + \frac{1}{2} \sum_{J=1}^{N} W_J \sigma_J^0 F_{IJ}^{k_t} \right] \Delta t, \qquad I = 1, ...N \tag{3.37}$$

The constant potential, ϕ_0, can be computed from Eq.(3.14) by employing the Gaussian quadrature,

$$\phi_0 = -\frac{1}{4\pi}\sum_{J=1}^{N} W_J \gamma_J \left(\frac{1}{|Q_J|} + \frac{1}{|Q'_J|}\right) \tag{3.38}$$

Chapter 4

Numerical Results

4.1 Hemisphere

Since the singularity occurs only in the $1/r$ term, it is important to validate the desingularization of the integral equation with the $1/r$ term only before it is applied to the time-domain integration. The numerical scheme is applied to the problem of uniform flow ($U = -1.0$) past a spheric surface ($R = 1.0$). Due to the symmetry, only one-half of the surface is considered. In Figure 4.1, dashed lines represent the control net of NURBS with 4×4 control points on one of patches ($N_p = 2$). The solid mesh forms the surface of one-quarter of the sphere generated by the control net. The perturbation velocity potentials at the Gaussian quadrature points were computed using both the NURBS and the analytical descriptions of the surface. The convergence of numerical solution was also investigated by varying the number of Gaussian quadrature points (NxN) over the hemisphere. The root-mean-square

(RMS) errors of the computed velocity potentials based on the analytical expression and the NURBS representation of the surface are shown in Figure 4.2. It is shown that the computed velocity potentials converge to the analytical solution as the number of Gaussian quadrature points increased. The RMS error of the solution based on the NURBS representation is less than 1% when 10x10 Gaussian quadrature points are applied.

The heave added-mass of a floating hemisphere was computed at the short-wave limit (Newman, 1977). The nondimensional added-mass is 0.5037 for 16x16 Gaussian quadrature points, compared with the analytical solution 0.5 (Havelock, 1955) and 0.517 for the panel method computed by SEALOADS with 256 flat panels over a hemisphere (Qiu and Hsiung, 1999).

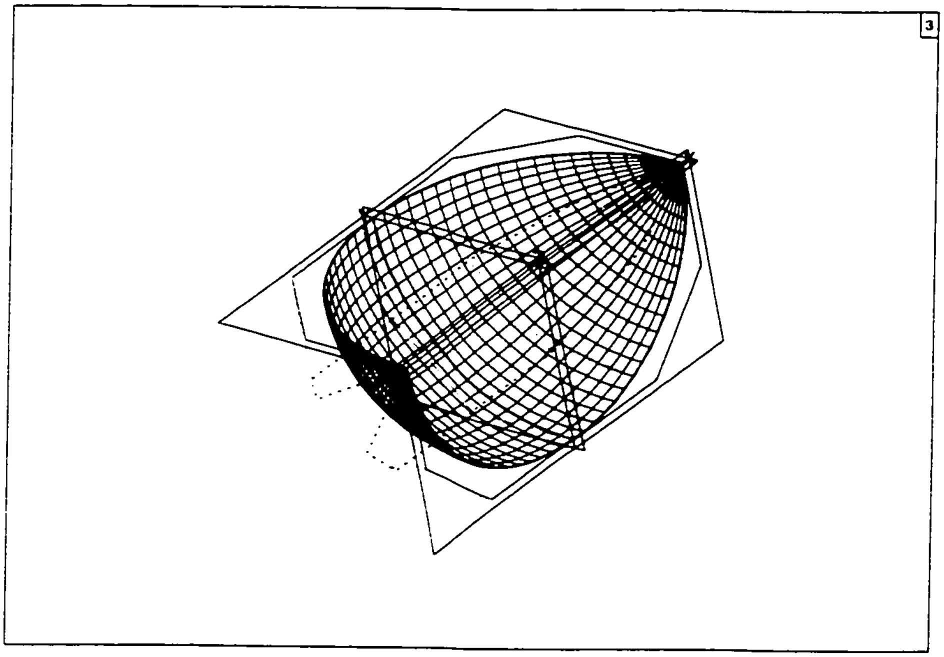

Figure 4.1: Spheric surface and control net

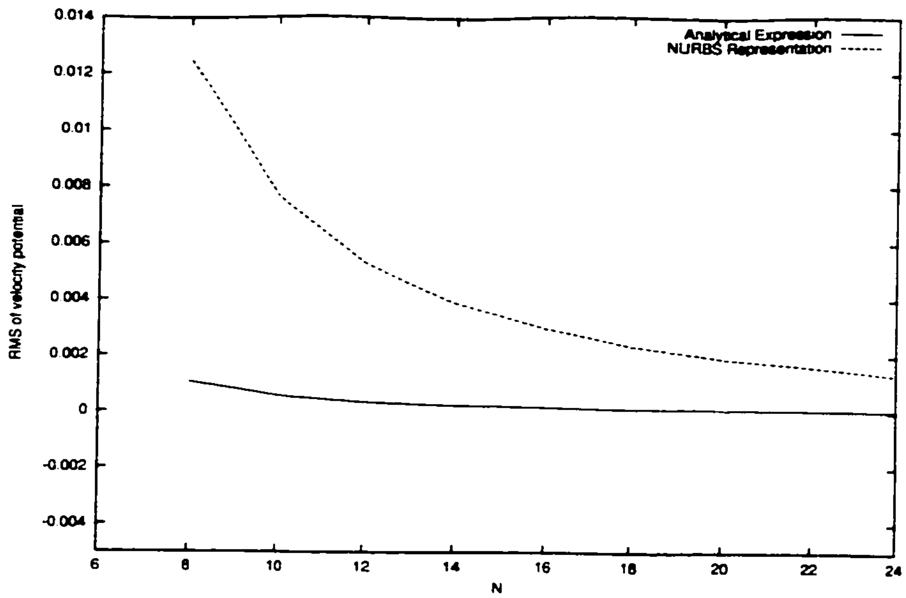

Figure 4.2: Convergence of numerical solution to the number of Gaussian quadrature points

4.1.1 The Radiation Problem

The panel-free method (PFM) was applied to compute the radiation response function for a hemisphere (R=5.0m) in heave. Figure 4.3 shows the nondimensional response function. $K_{33}(t)/(\rho\nabla)\sqrt{R/g}$. versus nondimensional time, $t\sqrt{g/R}$. for different Gaussian quadrature discretization used on the hemisphere, where R is the radius of the sphere and ∇ is the volume displacement. The time step, dt, was chosen as 0.05 second. The circles are the analytic solution of Barakat (1962) obtained by Fourier transform from his frequency-domain results. In this case, 4x4 Gaussian quadrature points were also employed to illustrate the numerical errors. It can be seen that an excellent agreement between the results by PFM and those from the analytical solution was achieved when 8x8 Gaussian quadrature points were chosen.

The nondimensional response function for the hemisphere in heave was also computed using different time steps with 16x16 Gaussian quadrature points. As shown in Figure 4.4, PFM is not very sensitive to the size of time steps. Figure 4.5 and Figure 4.6 present the added-mass and damping coefficients versus the nondimensional frequency for the hemisphere in heave. The numerical results were obtained by Fourier transform from the response function using 16x16 Gaussian points as shown in Figure 4.3. and the analytical results were from Hulme (1982). As shown in these figures, the agreement is excellent. Also in these figures, the frequency, the added-mass and the damping coefficients are nondimensionalized as $\omega^2 R/g$, $A_{33}/(\frac{2}{3}\rho\pi R^3)$ and $B_{33}/(\frac{2}{3}\omega\rho\pi R^3)$, respectively.

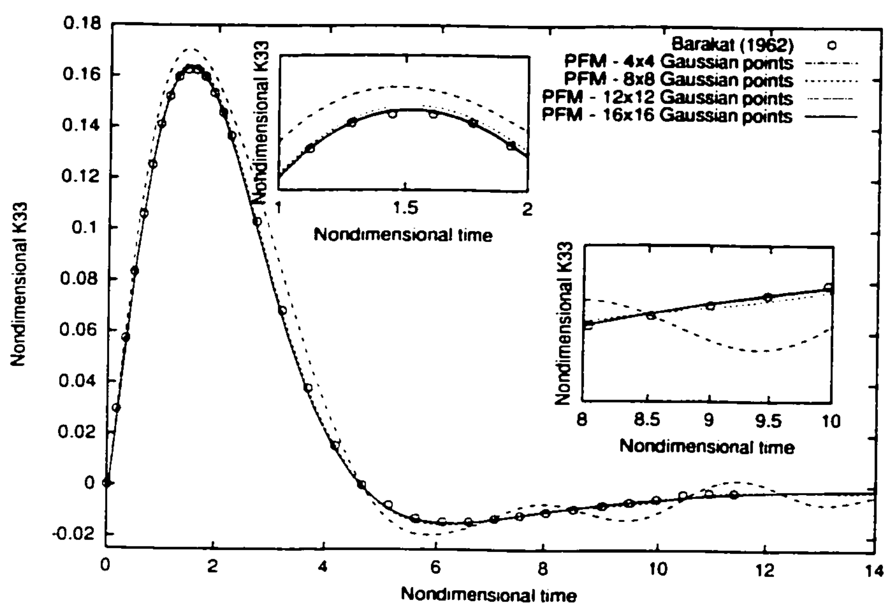

Figure 4.3: Nondimensional heave response function on a hemisphere versus nondimensional time (dt=0.05s)

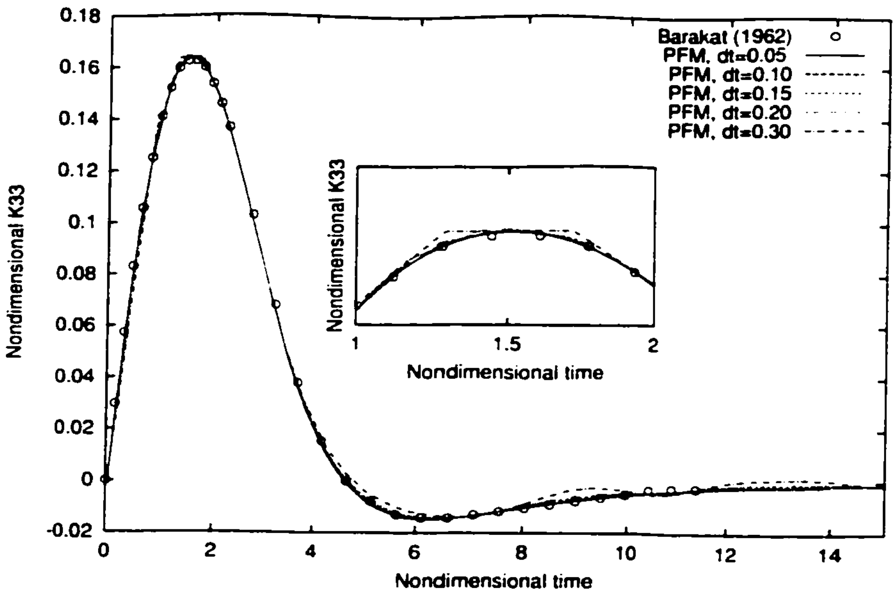

Figure 4.4: Nondimensional heave response function on a hemisphere versus nondimensional time (16x16 Gaussian points)

4.1.2 The Diffraction Problem

The computed diffraction response functions for sway and heave are nondimensionalized as $K_{27}(t)/(\rho g R\sqrt{gR})$ and $K_{37}(t)/(\rho g R\sqrt{gR})$, respectively, where ρ is the water density. They are given in Figures 4.7 and 4.8 versus nondimensional time, $t\sqrt{g/R}$. In these figures, a series of Gaussian points (8×8, 16×16, 8×16 and 8×32) were used to demonstrate the convergence of PFM to the number and arrangement of Gaussian points. The time step was chosen as 0.1 second. The circles are the computed results by King (1987) where a quarter of the hemisphere was approximated by 65 panels. It is seen that the oscillation at both ends of the response function curve tends to disappear when the number of Gaussian points increases. Compared with the response function for sway, the heave response function is not very sensitive to the number and arrangement of Gaussian points. More Gaussian points are needed along

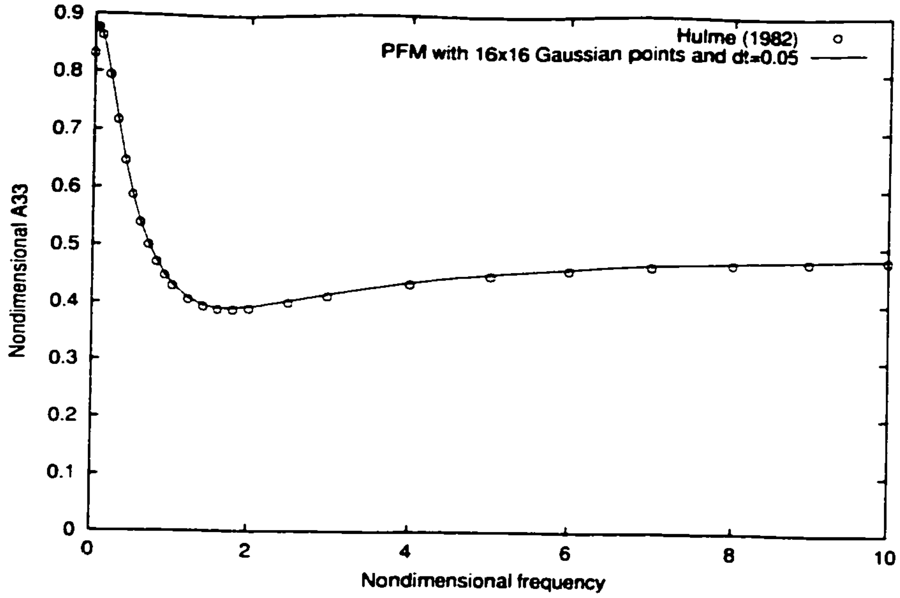

Figure 4.5: Nondimensional added-mass for a hemisphere in heave versus nondimensional frequency (dt=0.05s, 16x16 Gaussian points)

the x-direction for computation of the sway response function. The nondimensional response functions for sway and heave were also computed using different time steps with 8x16 Gaussian points. As shown in Figures 4.9 and 4.10, the response function for heave is again not very sensitive to the size of time steps.

The diffraction forces for heave and sway were then computed from the Fourier transformation of response functions (dt=0.05s) and compared with results from Haskind (1946), Cohen (1986) and King (1987). Figures 4.11 and 4.12 show the nondimensional heave diffraction forces, $F_3/(2\rho g\pi R^2)$ and phases versus the nondimensional frequency, kR, where k is again the wave number. The nondimensional sway diffraction forces and their phases are given in Figures 4.13 and 4.14. It can be seen that the computed diffraction forces and phases by PFM agree well with those results from Haskind (1946), Cohen (1986) and King (1987).

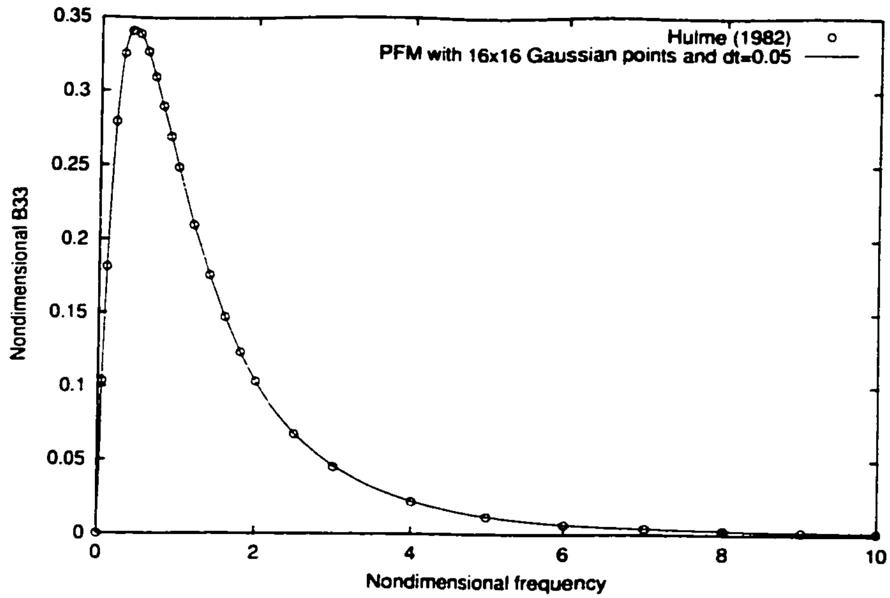

Figure 4.6: Nondimensional damping coefficient for a hemisphere in heave versus nondimensional frequency (dt=0.05s, 16x16 Gaussian points)

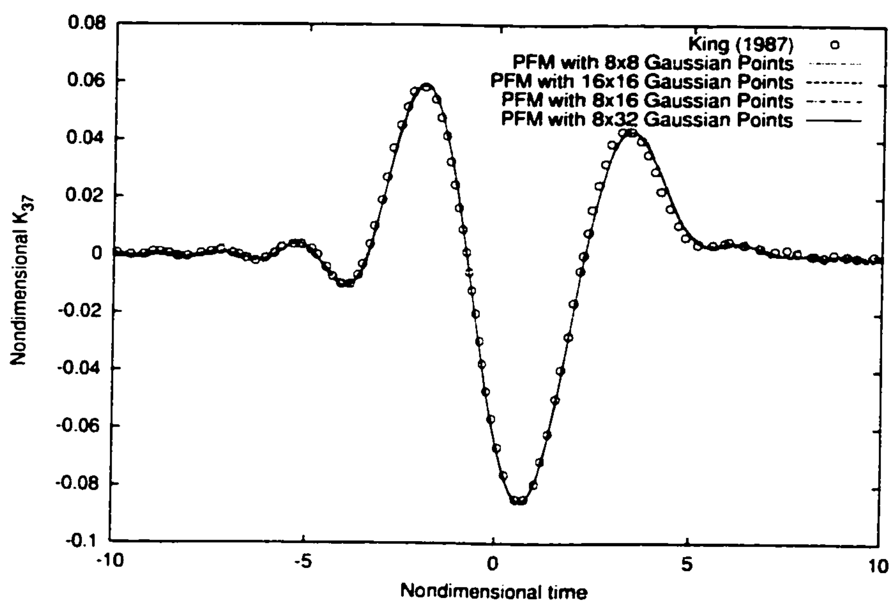

Figure 4.7: Nondimensional diffraction force response function for a hemisphere in heave (dt=0.1s)

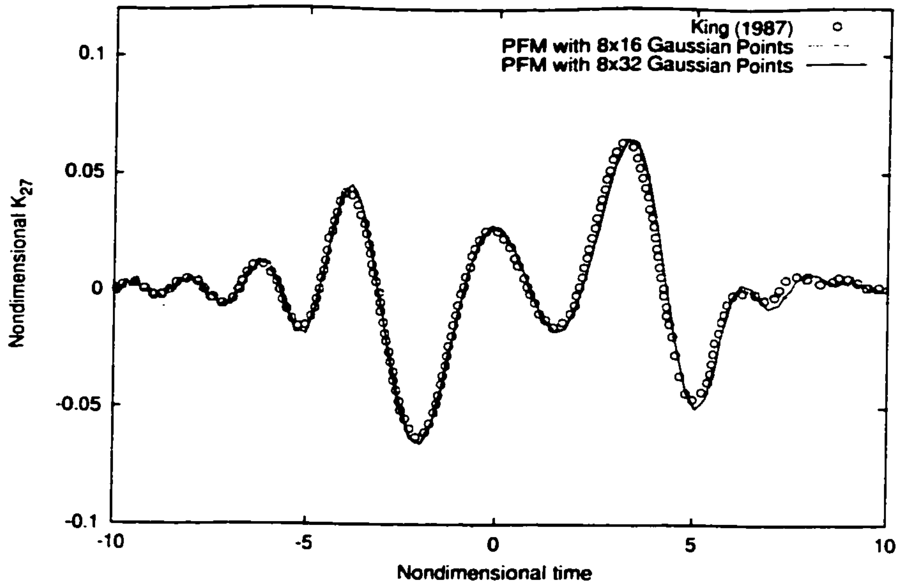

Figure 4.8: Nondimensional diffraction force response function for a hemisphere in sway (dt=0.1s)

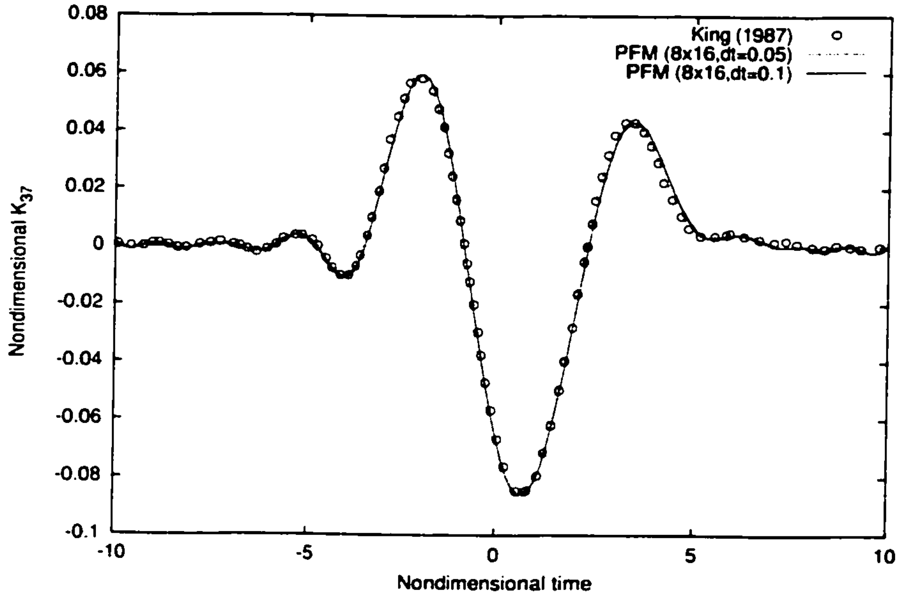

Figure 4.9: Nondimensional diffraction force response function for a hemisphere in heave (8×16 Gaussian points)

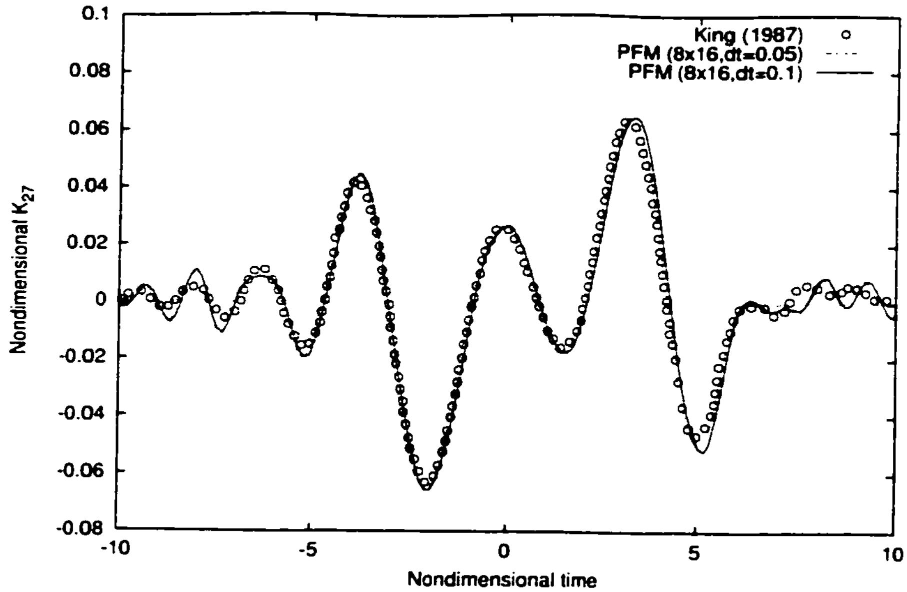

Figure 4.10: Nondimensional diffraction force response function for a hemisphere in sway (8×16 Gaussian points)

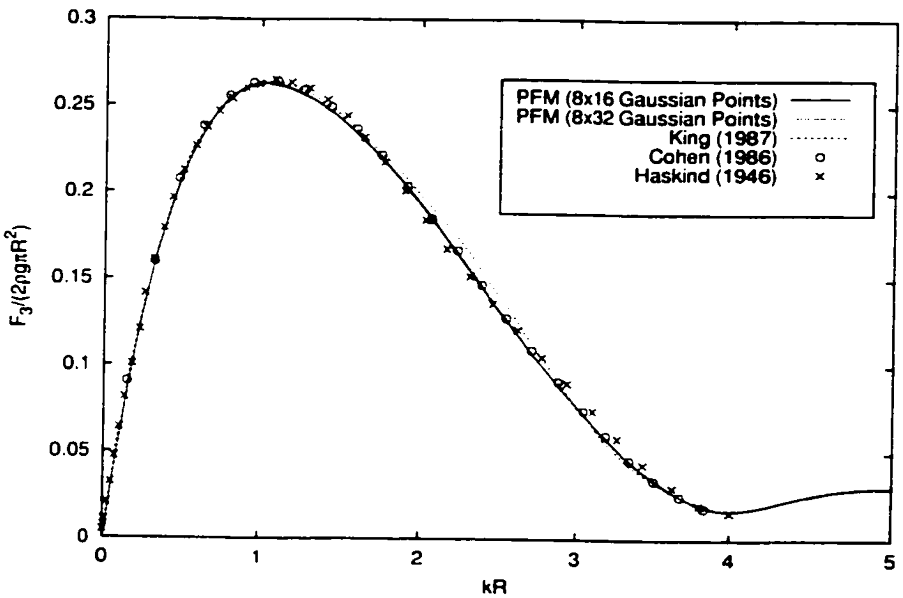

Figure 4.11: Nondimensional heave diffraction force for a hemisphere (dt=0.05s)

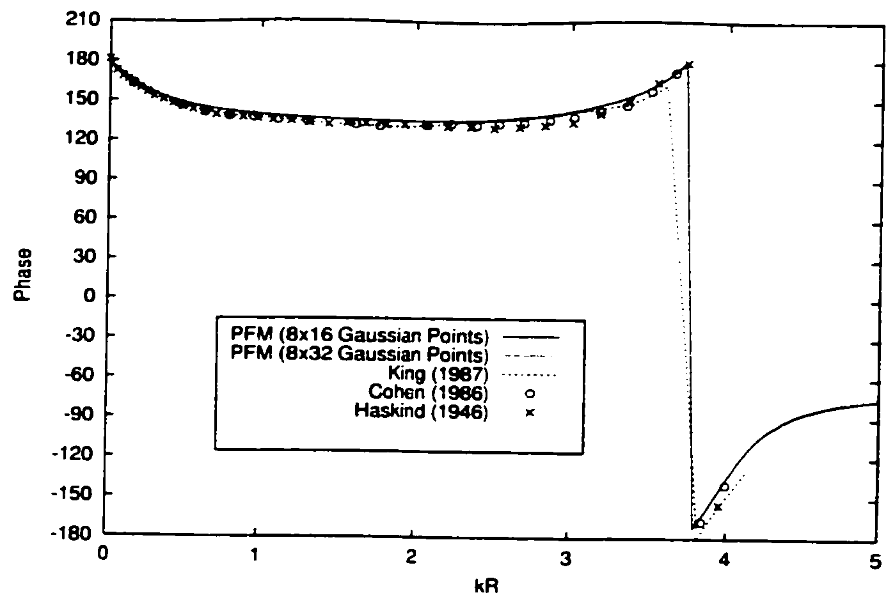

Figure 4.12: Phase of heave diffraction force for a hemisphere (dt=0.05s)

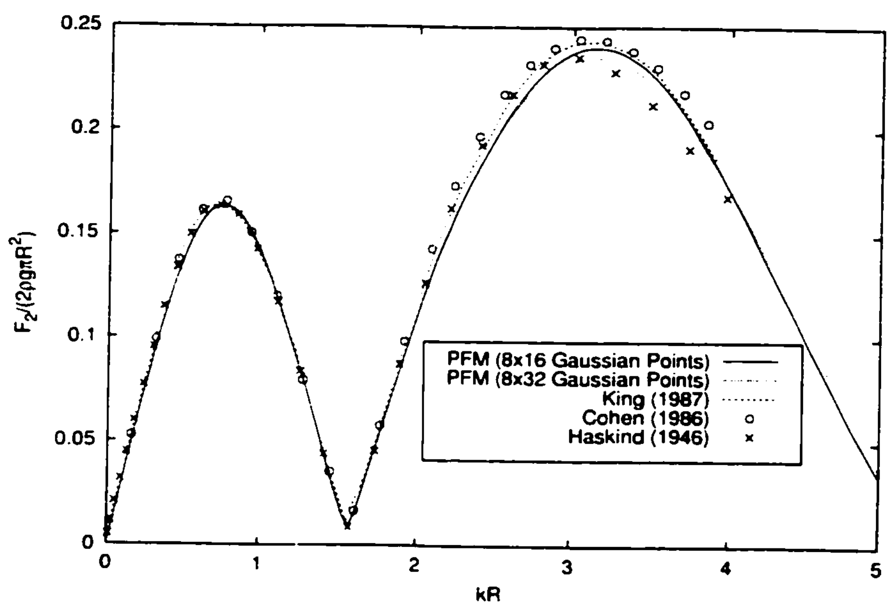

Figure 4.13: Nondimensional sway diffraction force for a hemisphere (dt=0.05s)

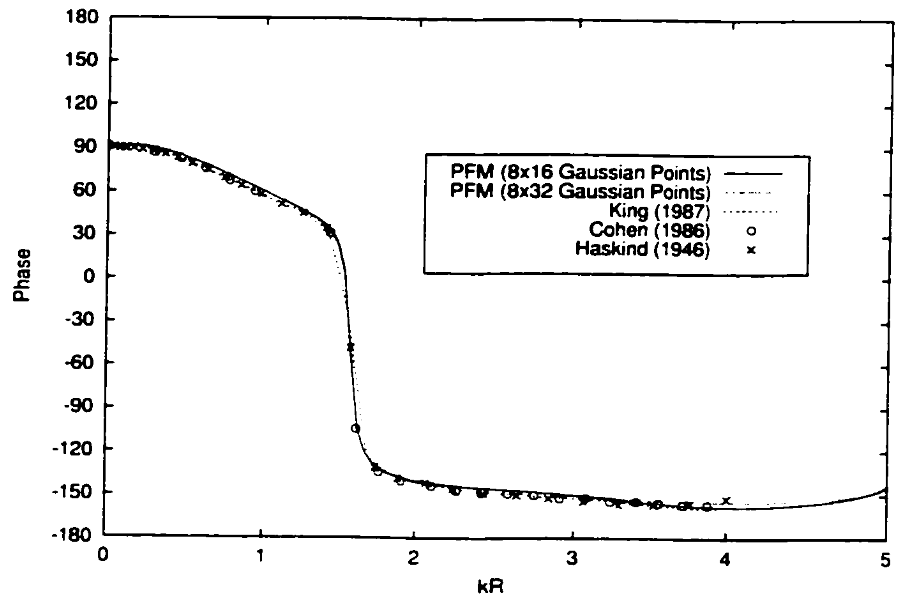

Figure 4.14: Phase of sway diffraction force for a hemisphere (dt=0.05s)

4.2 The Wigley Hull

The PFM was applied to a Wigley hull at zero speed. The hull geometry is defined by the equation:

$$\eta = (1-\zeta^2)(1-\xi^2)(1+0.2\xi^2)+\zeta^2(1-\zeta^8)(1-\xi^2)^4 \tag{4.1}$$

where the nondimensional variables are given by

$$\xi = \frac{2x}{L}, \quad \eta = \frac{2y}{B}, \quad \zeta = \frac{z}{T} \tag{4.2}$$

where L is the ship's length, B is the beam, and T is the draft. The hull used here has

$$\frac{L}{B} = 10, \quad \frac{L}{T} = 16, \quad L = 120.0 \tag{4.3}$$

and a block coefficient of

$$C_b = \frac{\nabla}{LBT} = 0.5606 \tag{4.4}$$

where ∇ is the volume displacement. Figures 4.15 and 4.16 shows the half of control nets and the corresponding whole body surface generated by the NURBS control nets, respectively.

4.2.1 Results of the Radiation Problem

A convergence test has been carried out for the Wigley hull by using various number of Gaussian points and arrangements. The computed heave and pitch response functions are more sensitive to the number of points on a cross-section than to the number of points along the ship length. At a given number of points on a cross-section, the results are almost unchanged when increasing the number of points along ship-length direction. It was again found that the computation is not sensitive to the time step. Figure 4.17 shows the computed heave response function at a time step $dt = 0.2s$ for two cases of using 18 and 20 Gaussian points on a cross-section, i.e. 9 and 10 points on one half of the cross-section, and 32 points along the ship length. Figure 4.18 shows the computed pitch response function. In these figures, the heave and pitch response functions, K_{33} and K_{55}, are nondimensionalized as $K_{33}/(\rho g\nabla/L)\sqrt{g/L}$ and $K_{55}/(\rho g\nabla)\sqrt{g/L}$, respectively. The time t is nondimensionalized as $t\sqrt{g/L}$.

The heave and pitch added-mass for the Wigley hull at Fn=0.0 were also computed from the response function. The heave added-mass and the frequency are nondimensionalized as $A_{33}/(\rho\nabla)$ and $\bar{\omega} = \omega\sqrt{g/L}$, respectively. The results from PFM were compared with results of TiMIT (Bingham, 1994) and WAMIT (Korsmeyer *et al.*, 1988). TiMIT and WAMIT are two panel-method codes from MIT for time-domain and frequency-domain wave analysis, respectively. Note that results of TiMIT and WAMIT used here were taken from the work of Bingham (1994). Figure 4.19 shows the comparison. The numerical irregular frequencies are shown at $\bar{\omega} \approx 5.8$ and $\bar{\omega} \approx 10$

for both TiMIT and WAMIT where the half-hull was discretized by 144 panels. PFM shows an oscillation around $\bar{\omega} = 5.8$, but its behavior is different from those of TiMIT and WAMIT.

The computed heave and pitch damping coefficients were also compared with those by Bingham (1994) in Figures 4.20 and 4.21. The heave and pitch damping coefficient is nondimensionalized as $B_{33}/(\rho\nabla\bar{\omega})\sqrt{L/g}$ and $B_{55}/(\rho\nabla L\bar{\omega})\sqrt{L/g}$, respectively.

4.2.2 Results of the Diffraction Problem

The wave exciting forces were determined at zero speed for the Wigley hull. The heave and pitch response functions for the Froude-Krylov forces were computed according to the work by King (1987). Then the exciting forces were compared with results from King (1987), where 120 panels were used to approximated the half-hull. In PFM computation, 18x32 Gaussian points were again used on the whole hull as in the radiation problem previously and the time step is 0.25s. The computed heave response function due to the diffracted waves in comparison with King's results is presented in Figure 4.22. The oscillation of the curve shown in results by the panel method is not presented in the results by PFM. The pitch response function is shown in Figure 4.23.

Applying Fourier transform to the diffraction and Froude-Krylov response functions, we were able to obtain the frequency-domain wave exciting forces. The forces and phases were compared with those results from King (1987) and the strip theory results of Salvesen *et al.* (1970) in Figures 4.24 to 4.27. To be consistent with the presentation of King (1987), the frequency is nondimensionalized as $\bar{\omega} = kL$, and the nondimensional heave and pitch exciting forces are given as $F_{37}/(\rho g \nabla / L)$ and $F_{57}/(\rho g \nabla)$, respectively. There is a good agreement between the results from PFM, the panel method and strip theory.

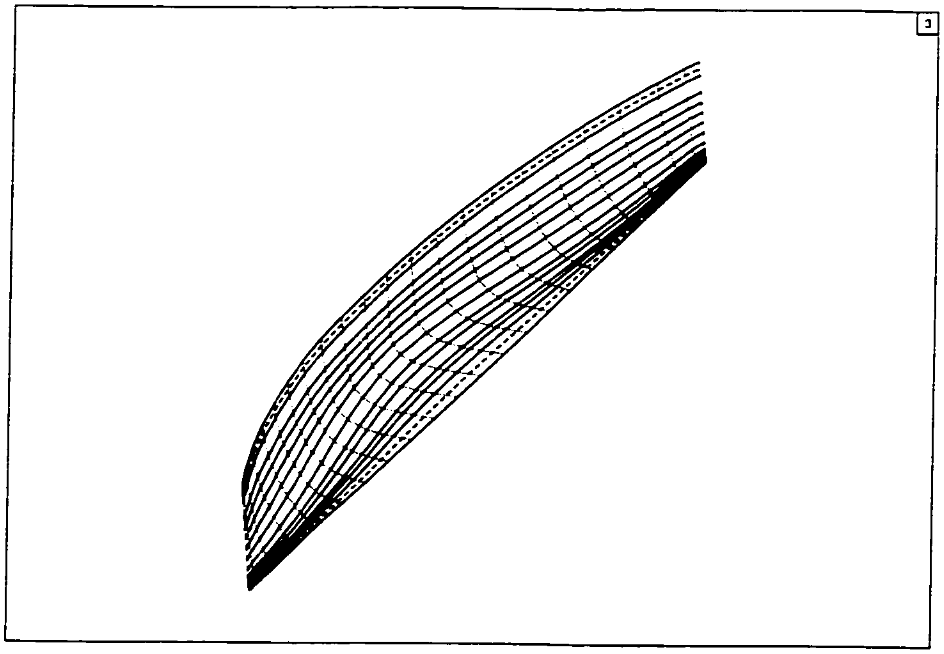

Figure 4.15: NURBS control net for the Wigley hull

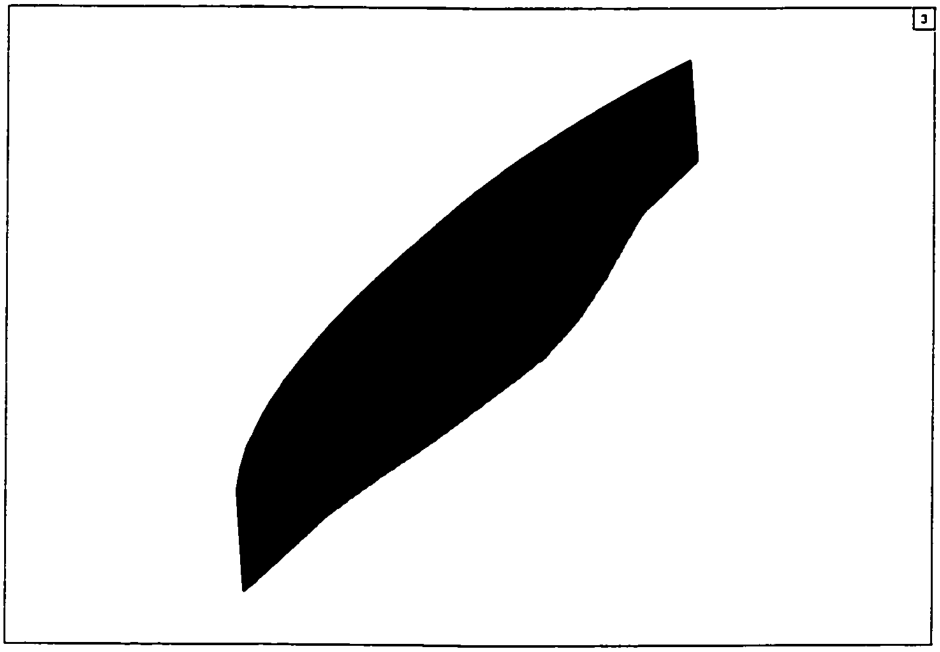

Figure 4.16: Wigley hull Surface generated by the NURBS control net

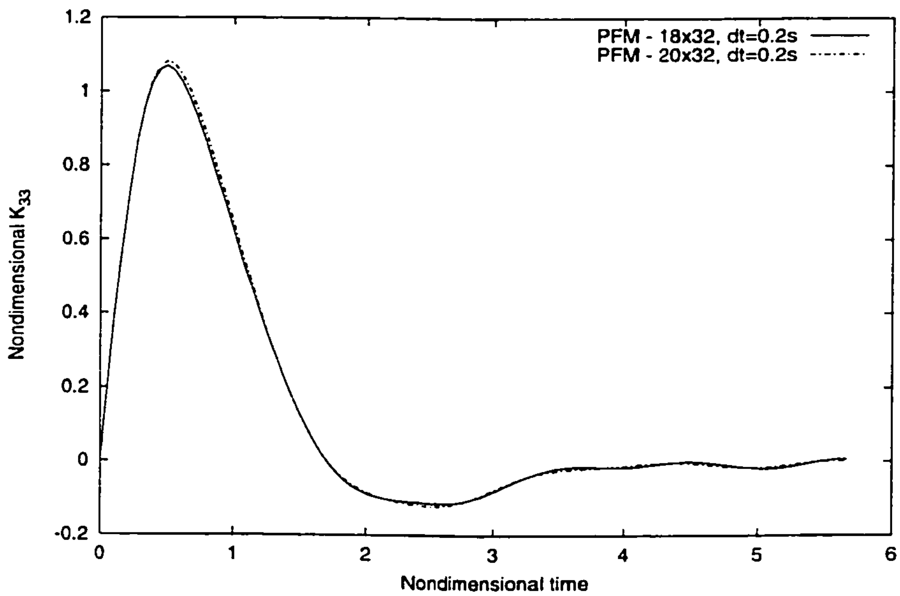

Figure 4.17: Heave radiation response function for the Wigley hull at Fn=0.0 (dt=0.2s)

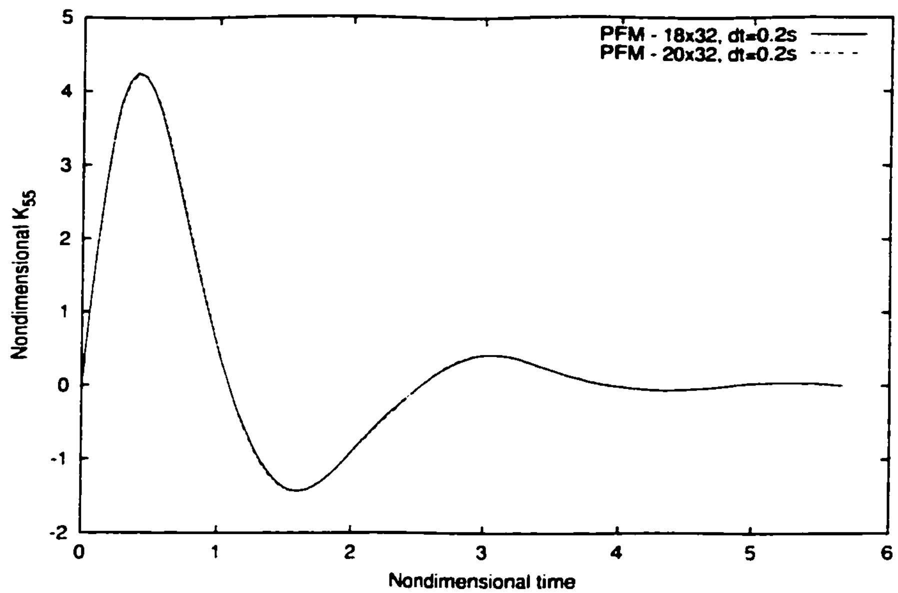

Figure 4.18: Pitch radiation response function for the Wigley hull at Fn=0.0 (dt=0.2s)

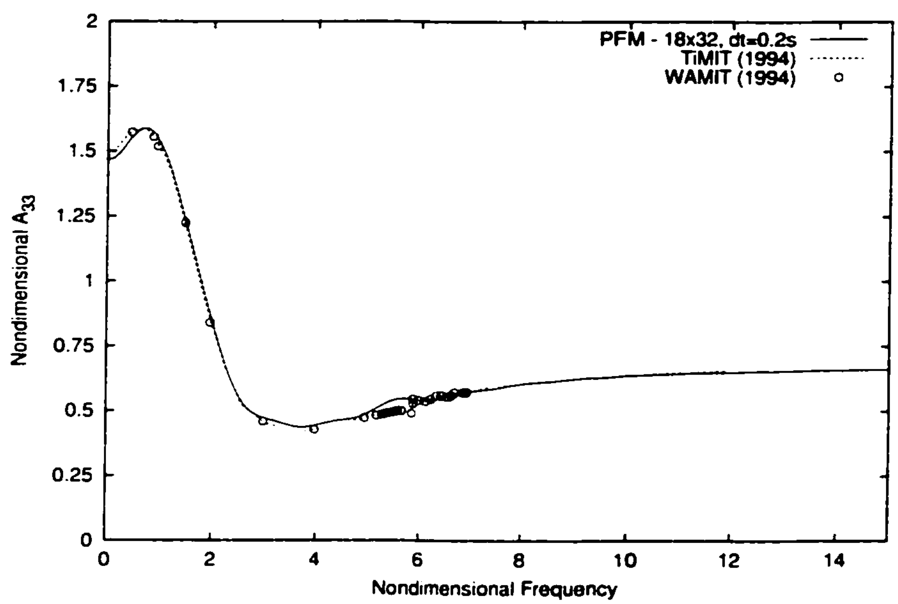

Figure 4.19: Heave added mass for the Wigley hull at Fn=0.0 (dt=0.2s)

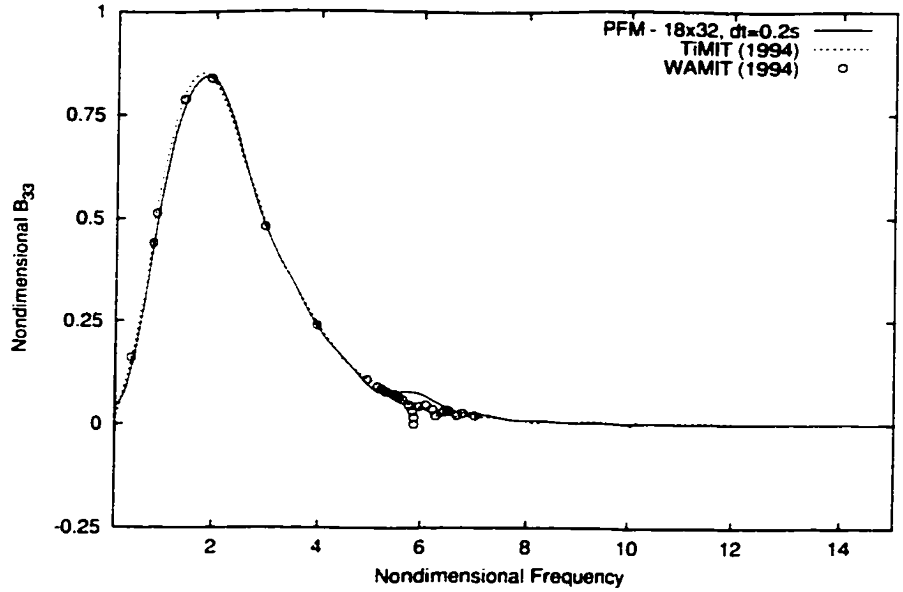

Figure 4.20: Heave damping coefficient for the Wigley hull at Fn=0.0 (dt=0.2s)

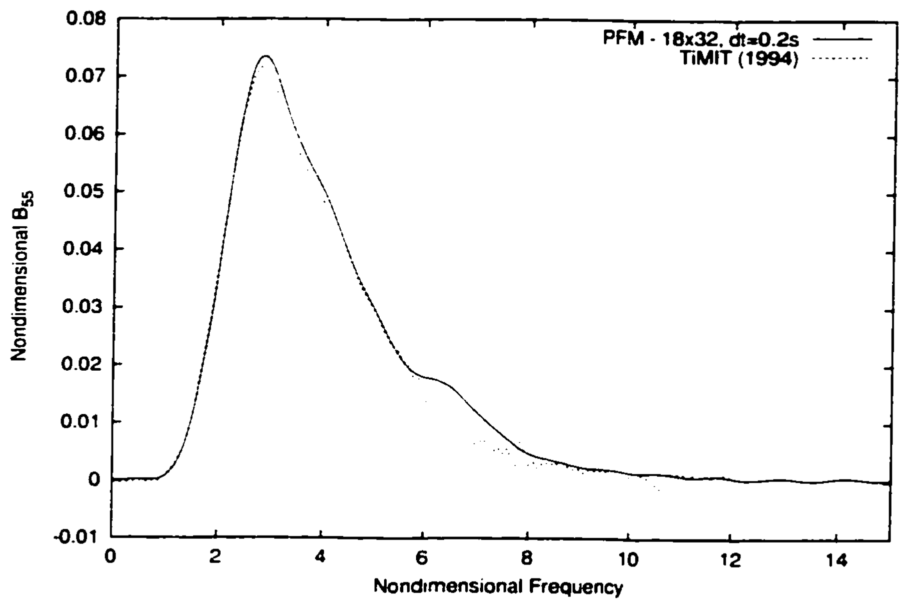

Figure 4.21: Pitch damping coefficient for the Wigley hull at Fn=0.0 (dt=0.2s)

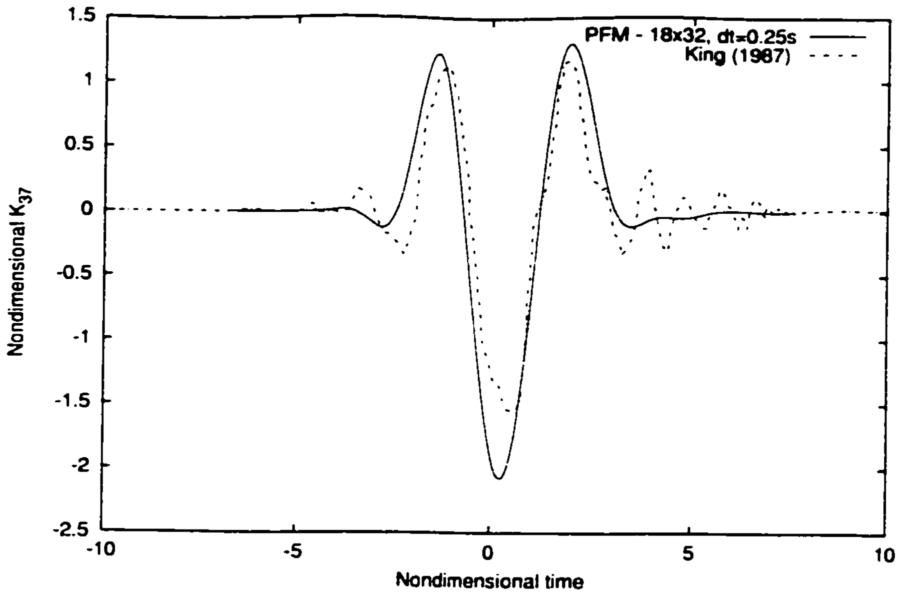

Figure 4.22: Heave response function due to diffracted waves for the Wigley hull at Fn=0.0 (dt=0.25s)

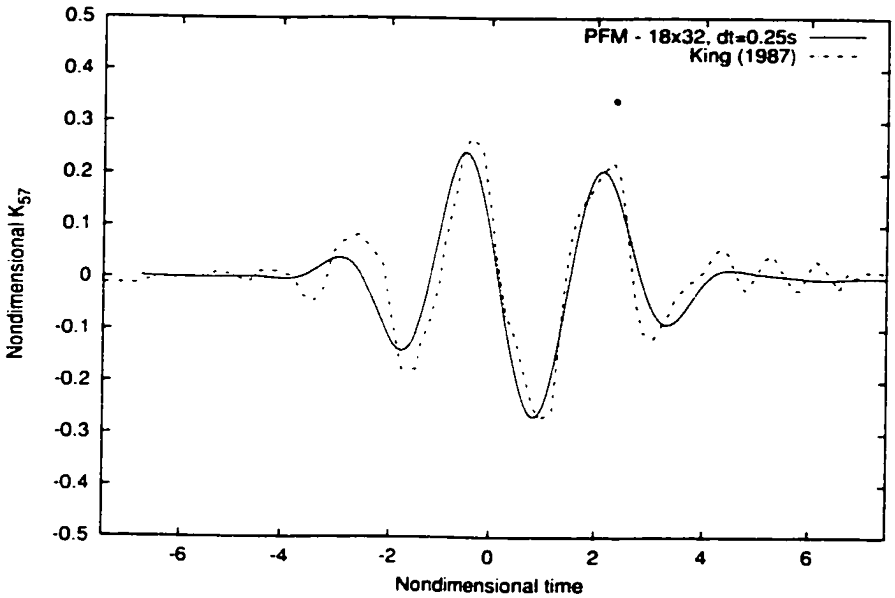

Figure 4.23: Pitch response function due to diffracted waves for the Wigley hull at Fn=0.0 (dt=0.25s)

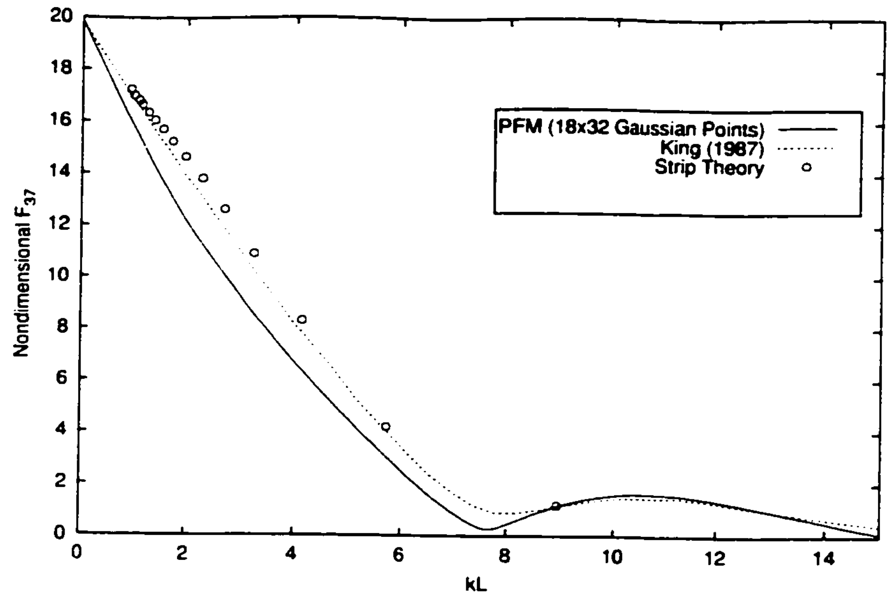

Figure 4.24: Heave exciting force for a Wigley hull at Fn=0.0 (dt=0.25s)

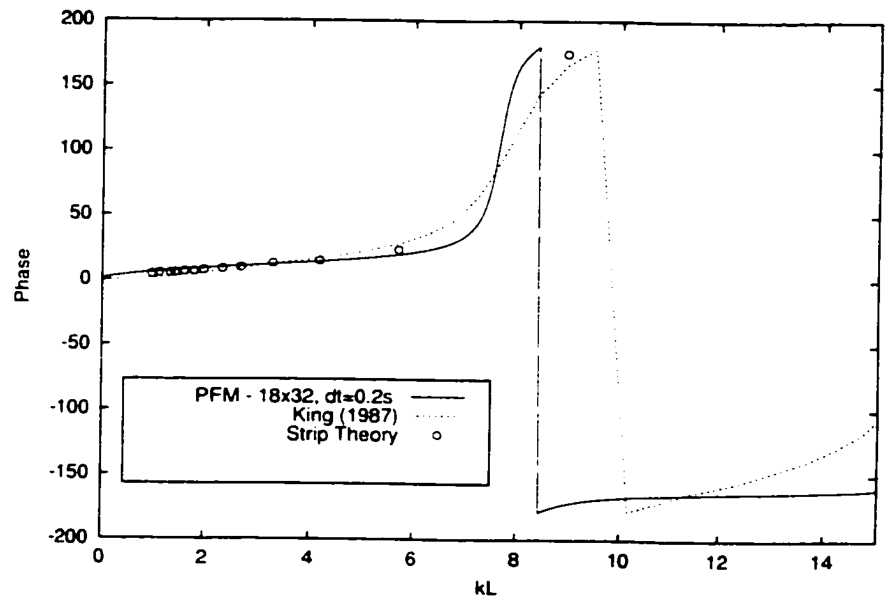

Figure 4.25: Heave exciting force phase for a Wigley hull at Fn=0.0 (dt=0.25s)

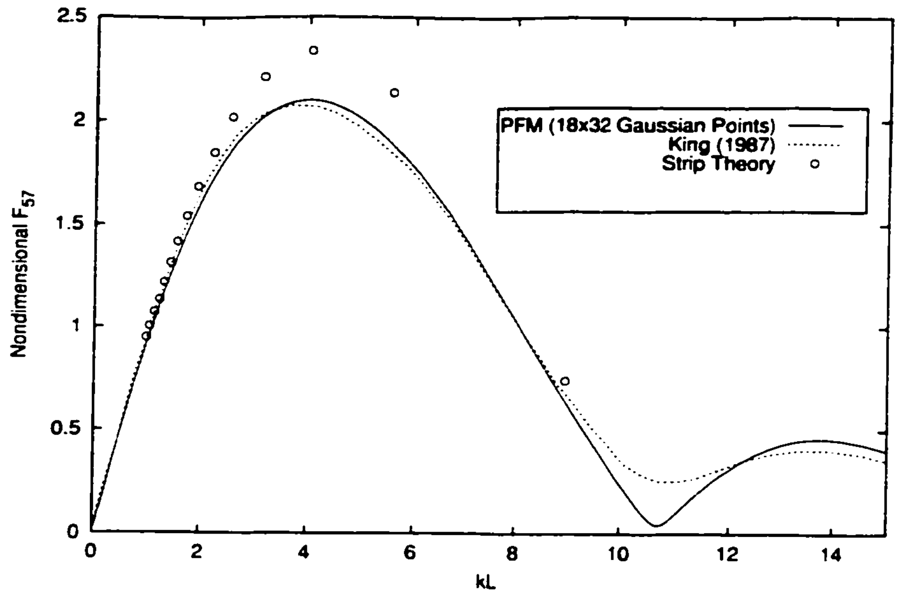

Figure 4.26: Pitch exciting force for a Wigley hull at Fn=0.0 (dt=0.25s)

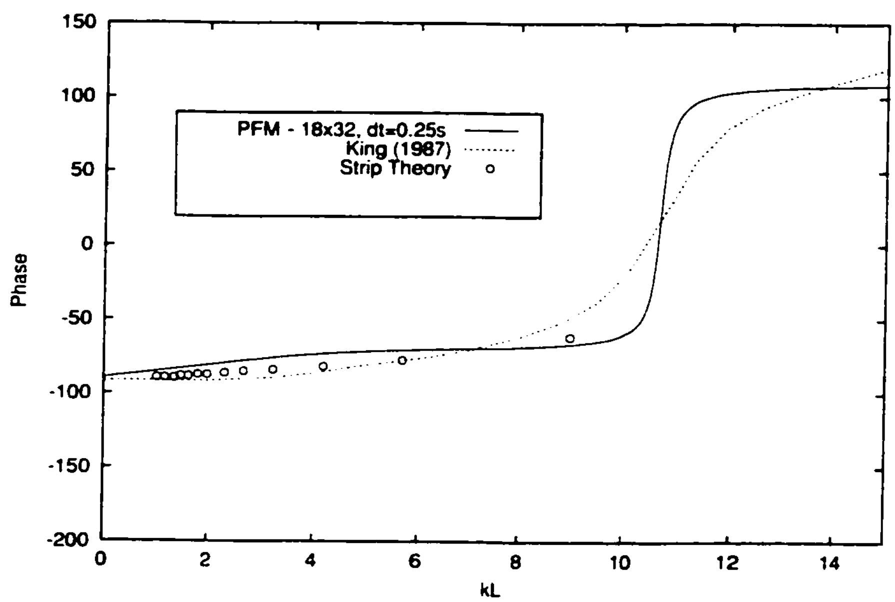

Figure 4.27: Pitch exciting force phase for a Wigley hull at Fn=0.0 (dt=0.25s)

Chapter 5

Conclusions and Recommendations

A panel-free method (PFM) has been developed to solve the radiation and diffraction problems in the time domain. The initial objective, to reduce the errors due to the geometry approximation and assumption of the degree of approximation of the source strength as in the panel method, has been achieved. In the present study, the integral equation in terms of source strength is desingularized before it is discretized. The singularity-free integral equation allows for application of Gaussian quadrature globally over the exact body geometry. The body geometry can be either described in an analytical definition or by a parametric representation. The complex body geometry may be accurately described by NURBS surfaces, which are widely used in computer aided design. There is no need to assume a certain degree of approximation of source strength distribution on the body surface.

In general, compared with the panel method, PFM involves less numerical manipulation, since panelization of a body surface is not needed. Programming of the PFM is easier than the panel method. It is more accurate, since the assumption for the degree of approximation of source strength distribution as in the panel method is no longer needed, and Gaussian quadrature can be directly and globally applied to the body surface with a mathematical description. The Gaussian quadrature points, and their respective Jacobian and normals on the surface can be accurately computed based on the NURBS expression. The accuracy of the solution can be easily enhanced and controlled by changing the number and arrangement of Gaussian quadrature points. This could lead to an adaptive error control of numerical computation for the three-dimensional boundary integral.

The robustness and accuracy of PFM has been demonstrated by its application to the radiation and diffraction problems in the time domain. The examples presented in Chapter 4 include the computation of radiation and diffraction response functions, hydrodynamic coefficients and wave exciting forces for a hemisphere and a Wigley hull.

A particular aspect which needs further research is the evaluation of the waterline integral by PFM. The waterline integral was omitted in the current work. In the panel method, the common practice was to evaluate the potential on the waterline as if the potential was on the body just below the waterline.

The PFM should be validated and improved by extending its applications to the cases of different types of ships for both with zero speed and forward speed. In the current work, PFM was applied to floating bodies with zero speed. Finally, the method as developed so far allows for computation of large-amplitude motions in the time domain. A challenging work related to applying PFM to the body-exact problem will be how to trim the control net for the instantaneous wetted surface of a floating body.

Appendix A

Numerical Solution of Response Functions

As shown in Eq.(2.57) and Eq.(2.63), the impulse response functions can be solved from the Fredholm integral equation of the first kind. Here, we define a general equation

$$F_r(t) = \int_{t_1}^{t_2} K_r(t-\tau)\eta_I d\tau \tag{A.1}$$

where

$F_r(t) = \dot{g}_{jk}(t) + h_{jk}(t) - \bar{\mu}_{jk}\ddot{\xi}_k(t) - \bar{\lambda}_{jk}\dot{\xi}_k(t) - \bar{\gamma}_{jk}\xi_k(t)$ for the radiation force,

$F_r(t) = -\dot{g}_{j7}(t) - h_{j7}(t)$ for the diffraction force,

and

$K_r = K_{jk}^R(P;t)$, $\eta_I = \dot{\xi}_k(t)$, $t_1 = 0$, $t_2 = t$ for the radiation problem,

$K_r = K_{j7}^D(P;t)$, $\eta_I = \bar{\eta}_0(t)$, $t_1 = -\infty$, $t_2 = \infty$ for the diffraction problem.

Equation(A.1) can be solved by the direct solution scheme (Cong, *et al.*, 1998). The convolution equation can be discretized as

$$F_{r_m} = \sum_{n=1}^{m-1} K_{r_{m-n}} \eta_{I_n} \Delta t + \frac{1}{2}[K_{r_m}\eta_{I_0} + K_{r_0}\eta_{I_m}]\Delta t, \quad m = 1, 2, ..., M \tag{A.2}$$

where M is the total number of steps defined by $t_M = M\Delta t$. With simplified notations,

$$\begin{cases} a_m &= \eta_{I_m} \\ x_m &= K_{r_m} \\ b_m &= F_{r_m} \end{cases}$$

Equation (A.2) becomes a system of equations in terms of x_m,

$$\begin{cases} \frac{1}{2}a_1x_0 + \frac{1}{2}a_0x_1 = \frac{b_1}{\Delta t} \\ \frac{1}{2}a_2x_0 + a_1x_1 + \frac{1}{2}a_0x_2 = \frac{b_2}{\Delta t} \\ \cdots \qquad = \ldots \\ \frac{1}{2}a_Mx_0 + a_{M-1}x_1 + \ldots + a_1x_{M-1} + \frac{1}{2}a_0x_M = \frac{b_M}{\Delta t} \end{cases} \tag{A.3}$$

It is evident that the systems of equations (A.3) are indeterminate, because the total number of unknowns M is larger than the total number of equations by 1. An additional physical condition has to be provided to make (A.3) closed. When time $t_m = m\Delta t$ is sufficiently long, the response function K_{r_m} becomes quite smooth and goes to zero uniformly, i.e, the first-order time derivative of K_{r_m} tends to zero. An additional condition for K_{r_m} at a specific time instant can be obtained by approximating the time derivative with a third-order finite difference, as follows:

$$x_{N-4} - 3x_{N-3} + 3x_{N-2} + x_{N-1} = 0, \quad \text{for} \quad N = M + 1 \tag{A.4}$$

Appendix B

Surface Construction Using NURBS

As mentioned in Chapter 3, the use of Non-Uniform Rational B-splines (NURBS) in surface constructions is becoming widespread. NURBS offers one common mathematical form for the precise representation of standard analytical shapes, such as lines, conics, circles and quadratic surfaces, as well as free-form curves and surfaces. NURBS curves and surfaces have been an Initial Graphic Exchange Specification (IGES) standard since 1983 (IGES, 1986). NURBS offers extra degrees of freedom, weights, to generate a large variety of shapes. It is projectively invariant, i.e., a projective transformation of the control points is equivalent to the transformation of the corresponding curve or surfaces. In this Appendix, the basic theory of NURBS will be briefly outlined. As an example, the NURBS description of a sphere will be presented.

B.1 Rational and Non-Rational B-Splines Curves and Surfaces

B.1.1 B-Spline Basis Functions

The recursive B-Spline basis functions, as in Eq.(3.16) and Eq.(3.17), are known as the Cox-deBoor algorithm (Cox, 1972, deBoor, 1972). For a non-decreasing sequence of real number, $\mathbf{U} = \{u_0, u_1, ...t_i, ..., u_m\}$, the ith normalized B-spline function of degree p can be written as follows:

$$N_{i,0}(u) = \begin{cases} 1 & \text{if } u_i \leq u < u_{i+1} \\ 0 & \text{otherwise} \end{cases} \tag{B.1}$$

$$N_{i,p}(u) = \frac{u - u_i}{u_{i+p} - u_i} N_{i,p-1}(u) + \frac{u_{i+p+1} - u}{u_{i+p+1} - u_{i+1}} N_{i+1,p-1}(u) \tag{B.2}$$

It has been set that 0/0=0. The $N_{i,p}$ functions are defined on the entire domain, but the focus is on the interval $u \in [u_0, u_m]$. Note that $\mathbf{U}$ is called the knot vector and $N_{i,p}(u)$ is the pth degree piecewise polynomial function. In Figure B.1, (a) shows the quadratic B-spline basis functions defined by the knot vector $\{0, 0, 0, 1/3, 2/3, 1, 1, 1\}$ and (b) illustrates the cubic B-spline functions corresponding to the knot vector $\{0, 0, 0, 0, 1/4, 1/2, 3/4, 1, 1, 1, 1\}$. Note that Figure B.1 is cited from Piegl and Tiller (1987).

The shape of basis functions are not only controlled by the degree p, but also by

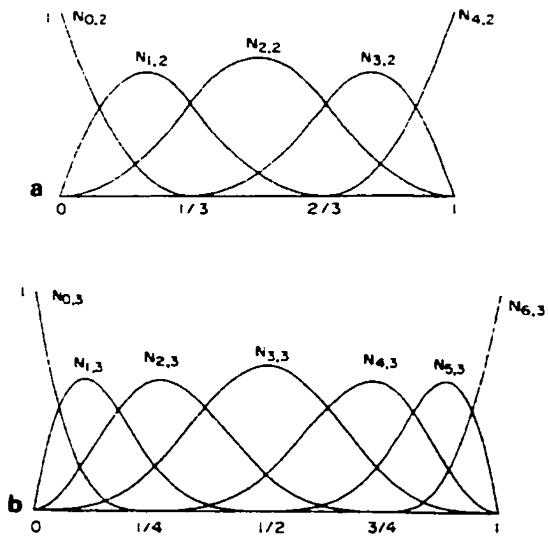

Figure B.1: Quadratic and cubic B-spline basis functions (Piegl and Tiller. 1987)

the knot vector. $\mathbf{U}$. Various knot vectors can be chosen. Let's fix the degree of basis function as p. The knot vector. $\mathbf{U} = \{u_0, u_1, ...t_i, ..., u_m\}$, is non-periodic if the first and last knots are repeated with multiplicity $p+1$, i.e., $u_0 = u_1 = ... = u_p$ and $u_{m-p} = u_{m-p+1} = ... = u_m$. If there is a positive real number, Δu, such that $u_{i+1} - u_i = \Delta u$ for all $p \leq i \leq m-p-1$, then $\mathbf{U}$ is called a uniform knot vector. It is otherwise called the non-uniform knot vector. The use of the non-uniform knot vector allows better shape control than that of the uniform one. Furthermore, the use of uniform B-splines to interpolate unevenly spaced data point can result in unwanted oscillations or loops.

B.1.2 Non-Rational B-Spline Curves

A pth degree non-rational B-spline curve is defined as follows:

$$\mathbf{P}(u) = \sum_{i=0}^{n} N_{i,p}(u)C_i, \quad 0 \le u \le 1 \tag{B.3}$$

where the C_i are the control points, n is the number of control points, and the $N_{i,p}(u)$ are again the pth degree B-spline functions with a non-periodic knot vector, $\mathbf{U} = \{u_0, u_1, ...t_i, ..., u_m\}$, where $m = n + p + 1$.

The multiplicity $(p+1)$ of the end knots yields the end conditions as follows:

$$P(0) = C_0, \quad P(1) = C_n, \quad P'(0) = p(C_1 - C_0)/u_{p+1}, \tag{B.4}$$
$$\text{and} \quad P'(1) = p(C_n - C_{n-1})/(1 - u_{m-p-1})$$

B.1.3 Rational B-Spline Curves

A point $P(x, y, z)$ in the Cartesian coordinate system can be represented by $P^w(wx, wy, wz, w), w > 0$ in the four-dimensional (4D) space. The normalization is a perspective mapping defined as follows:

$$H\{P^w(wx, wy, wz, w)\} = \begin{cases} P(wx/w, wy/w, wz/w) & \text{if } w \neq 0 \\ \text{Point at infinity on the line} & \\ \text{from the origin through}(x, y, z) & \text{if } w = 0 \end{cases} \tag{B.5}$$

The set of $P_i^w(w_ix_i, w_iy_i, w_iz_i, w_i)$, $i = 0, ..., n$, defines a non-rational B-spline curve in 4D. Note that $P(x, y, z) = P^w(x, y, z, 1)$. Its perspective map in 3D is a rational B-spline curve defined as follows:

$$\begin{aligned} P(u) &= H\{P^w(u)\} = H\{\sum_{i=0}^{n} N_{i,p}(u)C_i^w\} \\ &= \frac{\sum_{i=0}^{n} N_{i,p}(u)w_iC_i}{\sum_{i=0}^{n} N_{i,p}(u)w_i} = \sum_{i=0}^{n} N_{i,p}^R(u)C_i \end{aligned} \tag{B.6}$$

where the functions, $N_{i,p}^R(u)$, are piecewise rational basis functions and $w_i \geq 0$ for all value of i. It can be seen that $N_{i,p}^R(u)$ will reduce to $N_{i,p}(u)$ if all $w_i = 1$.

Figure B.2 illustrates rational cubic B-spline curves with different value of w_1 and w_2, where small squares represents the end points of the curve segments. As shown, when all $w_i = 1$, the curve reduces to a non-rational B-spline curve.

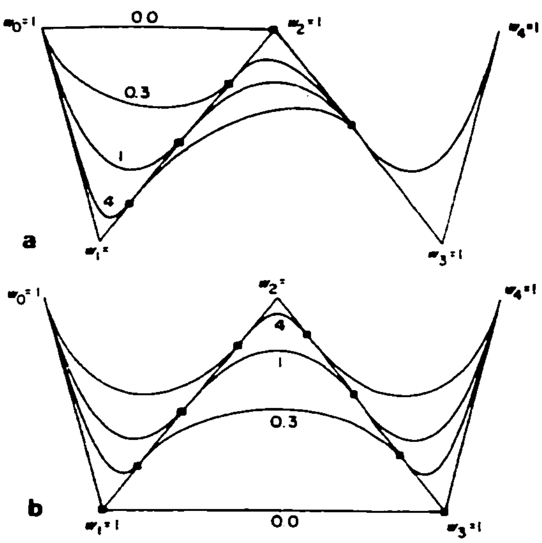

Figure B.2: Rational cubic B-spline curves with different values of w_1 and w_2 and their control polygon (Piegl and Tiller, 1987)

B.1.4 Rational B-Spline Surfaces

A curve requires one parameter for its definition, whereas a surface requires two: u and v for $0 \leq u, v \leq 1$. A tensor product rational B-spline surface with degrees (p, q) is defined as follows:

$$\begin{aligned} P(u,v) &= H\{P^w(u,v)\} = H\{\sum_{i=0}^{n}\sum_{j=0}^{m} N_{i,p}(u)N_{j,q}(v)C_{ij}^w\} \\ &= \frac{\sum_{i=0}^{n}\sum_{j=0}^{m} w_{ij}C_{i,j}N_{i,p}(u)N_{j,q}(v)}{\sum_{i=0}^{n}\sum_{j=0}^{m} w_{ij}N_{i,p}(u)N_{j,q}(v)} \end{aligned} \quad (B.7)$$

where C_{ij} denote the control points which are arranged in a topologically rectangular array called the control net.

B.2 NURBS surface of a Sphere

As an example, the control net of a sphere with radius 0.5 is given in Figure B.3 and its corresponding NURBS surface is presented in Figure B.4. In the example, a 4×4 control net and $p, q = 3$ are used for the NURBS surface. For a 1/8 sphere, the knot vectors, **U** and **V** are both given as $\{0, 0, 0, 0, 1, 1, 1, 1\}$. The coordinates (x,y,z) and weights (w) of control points are list in Table B.1.

For a complex body surface, such as a ship hull, the NURBS surface can be constructed by using NURBS surface modeling packages, such as FastShip^R, which has been used for generation of the Wigley hull.

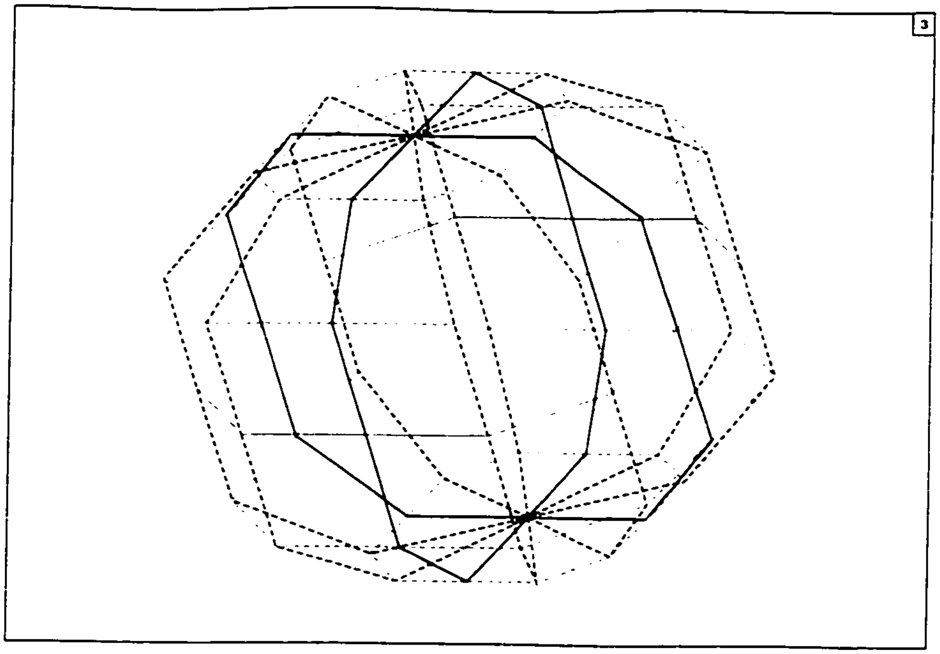

Figure B.3: Control net for the sphere

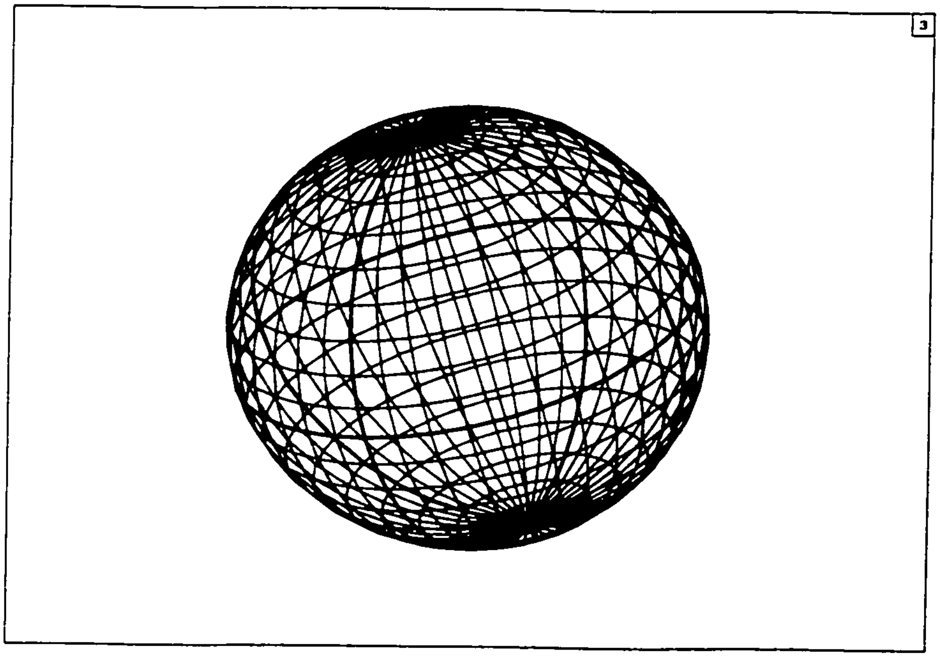

Figure B.4: NURBS spheric surface

Table B.1: Control net for the 1/8 sphere

Control Points	x	y	z	w
(1,1)	0.000000	0.500000	0.000000	1.000000
(1,2)	0.000000	0.500000	-0.292893	0.804738
(1,3)	0.000000	0.292893	-0.500000	0.804738
(1,4)	0.000000	0.000000	-0.500000	1.000000
(2,1)	0.292893	0.500000	0.000000	0.804738
(2,2)	0.292893	0.500000	-0.292893	0.647603
(2,3)	0.292893	0.292893	-0.500000	0.647603
(2,4)	0.292893	0.000000	-0.500000	0.804738
(3,1)	0.500000	0.292890	0.000000	0.804738
(3,2)	0.500000	0.292890	-0.171571	0.647603
(3,3)	0.500000	0.171571	-0.292890	0.647603
(3,4)	0.500000	0.000000	-0.292890	0.804738
(4,1)	0.500000	0.000000	0.000000	1.000000
(4,2)	0.500000	0.000000	0.000000	0.804738
(4,3)	0.500000	0.000000	0.000000	0.804738
(4,4)	0.500000	0.000000	0.000000	1.000000

References

Barakat, R. (1962). Vertical Motion of a Floating Sphere in a Sinewave Sea. Journal of Fluid Mechanics, Vol.13, pp. 540-556.

Beck, R. F., Cao, Y., Scorpio, S. M. and Schultz, W. W. (1994). Nonlinear Ship Motion Computations Using the Desingularized Method. Proceeding of 20th Symposium of Naval Hydrodynamics, Santa Barbara, CA, pp. 227-246.

Beck, R. F. and King, B. (1989). Time-Domain Analysis of Wave Exciting Forces on Floating Bodies at Zero Forward Speed. Applied Ocean Research, Vol. 11, pp. 19-25.

Beck, R. F. and Liapis, S. J. (1987). Transient Motion of Floating Bodies at Zero Forward Speed. Journal of Ship Research, Vol. 31, pp. 164-176.

Beck, R. F. and Magee, A. (1990). Time-Domain Analysis for Predicting Ship Motions. Proceedings of IUTAM Symposium, Dynamics of Marine Vehicles and Structures in Waves, London.

Chang, M. S. (1977). Computation of Three-Dimensional Ship-Motions with Forward Speed. Proceeding Second International Conference on Numerical Ship Hydrodynamics, University of California, Berkeley, pp. 124-135.

Cohen, S. B. (1986). A Time Domain Approach to Three-Dimensional Free Surface Hydrodynamic Interactions in Narrow Basins. Ph.D. Thesis, The University of Michigan, Ann Arbor, MI.

Cong, L.Z., Huang, Z.J., Ando, S. and Hsiung, C.C. (1998). Time-Domain Analysis of Ship Motions and Hydrodynamic Pressures on a Ship Hull in Waves. 2nd International Conference on Hydroelasticity in Marine Technology, Fukuoka, Japan.

Cox, M. (1972). The Numerical Evaluation of B-Splines. J. Inst. Maths. Applic., Vol. 10, pp. 134-149.

Cummins, W. E. (1962). The Impulse Response Function and Ship Motions. Schiffstechnik, Vol. 9, pp. 101-109.

deBoor, C. (1972). On Calculation with B-Splines. J. Approximation Theory, Vol. 6, pp. 50-62.

de Kat, J. O. (1990). The Numerical Modelling of Ship Motions and Capsizing in Severe Seas. Journal of Ship Research, Vol. 34, pp. 289-301.

Danmeier, D. G. (1999). A Higher-Order Panel Method for Large-Amplitude Simulation of Bodies in Waves. Ph.D. Thesis, Massachusetts Institute of Technology, Cambridge, MA.

Farin, G. E. (1991). NURBS for Curve and Surface Design. SIAM Activity Group on Geometric Design.

Finkelstein, A. (1957). The Initial Value Problem for Transient Water Waves. Communications on Pure and Applied Mathematics, Vol. 10, pp. 511-522.

Guevel, P. and Bougis, J. (1982). Ship Motions with Forward Speed in Infinite Depth. International Shipbuilding Progress, Vol. 29, No. 332, pp. 105-117.

Haskind, M. D. (1946). The Hydrodynamic Theory of Ship Oscillations in Rolling and Pitching. Prikl. Mat. Mekh., Vol. 10, pp. 33-66.

Havelock, T.H., (1955). Waves due to a Floating Sphere Making Periodic Heaving Oscillations. Proceedings of the Royal Society, A, Vol. 231, pp. 1-7.

Hess, J.L. and Smith, A.M.O. (1964). Calculation of Nonlifting Potential Flow about

Arbitrary Three-Dimensional Bodies. Journal of Ship Research, Vol. 8, No. 3, pp. 22-44.

Hsin, C.Y., Kerwin, J.E. and Newman, J.E. (1993). A Higher-Order Panel Method for Ship Motions Based on B-Splines. Proceeding of the Sixth International Conference on Numerical Ship Hydrodynamics, Iowa City, Iowa.

Holtrop, J. and Mennen, G. G. J. (1982). An Approximate Power Prediction Method. International Ship Building Progress, No. 335, Vol. 29.

Huang, Y. (1997). Nonlinear Ship Motions by a Rankine Panel Method. Ph.D. Thesis, Massachusetts Institute of Technology, Cambridge, MA.

IGES (1986). Initial Graphics Exchange Specification, Version 3.0. Document No. NBSIR 86-3359, National Bureau of Standards, Gaithersburg, MD, U.S.A.

Hulme, A. (1982). The Wave Forces Acting on a Floating Hemisphere Undergoing Forced Periodic Oscillations. Journal of Fluid Mechanics, Vol. 121, pp. 443-463.

Inglis, R. B. and Price, W. G. (1982). A Three-Dimensional Ship Motion Theory - Comparison between Theoretical Prediction and Experimental Data of the Hydrodynamic Coefficient with Forward Speed. Transaction Royal Institution of Naval Architecture, Vol. 124, pp. 141-157.

King, B. K. (1987). Time-Domain Analsyis of Wave Exciting Forces on Ship and Bodies. Ph.D. Thesis, The Univeristy of Michigan, Ann Arbor, MI.

King, B. K., Beck, R. F. and Magee, A.R. (1988). Seakeeping Calculations With Forward Speed Using Time Domain Analysis. Proceedings of the Seventeenth Symposium on Naval Hydrodynamics, The Hague, Netherlands.

Kouh, J.S. and Ho, C.H. (1996). A High Order Panel Method Based on Source Distribution and Gaussian Quadrature. Schiffstechnik Bd. Vol. 43, pp. 38-47.

Korsmeyer, F.T., Lee, C.H., Newman, J.N. and Sclavounos, P.D. (1988). The Analysis of Wave Effects on Tension-Leg Platforms. Proceeding of 7th International Conference on Offshore Mechanics and Arctic Engineering (OMAE). Houston. TX. pp. 1-14.

Landweber, L. and Macagno, M. (1969). Irrotational Flow about Ship Forms. IIHR Report, No. 123, The University of Iowa, Iowa City, Iowa.

Lee. C.H., Farina, L. and Newman, J.N. (1998). A Geometry-Independent Higher-Order Panel Method and Its Application to Wave-Body Interactions. Proceedings of Engineering Mathematics and Applications Conference. Adelaide.

Liapis. S. J. (1986). Time-Domain Analysis of Ship Motions. Ph.D. Thesis. The University of Michigan, Ann Arbor, MI.

Liapis, S. J. and Beck, R. F. (1985). Seakeeping Computations Using Time Domain Analysis. Proceedings of the Fourth International Conference on Numerical Ship Hydrodynamics, Washington. D.C.

Lin, W. M. and Yue, D. K. (1994). Large Amplitude Motions and Wave Loads for Ship Design. Proceedings of the 20th Symposium on Naval Hydrodynamics, Santa Barbara, California.

Lin. W. M. and Yue. D. K. (1990). Numerical Simulations for Large Amplitude Ship Motions in the Time Domain. Proceedings of the 18th Symposium on Naval Hydrodynamics. Ann Arbor, Michigan.

Maniar. H.D. (1995). A Three Dimensional Higher Order Panel Method Based on B-Splines. Ph.D. Thesis, Massachusetts Institute of Technology, Cambridge, MA.

Magee. A. (1994). Seakeeping Applications Using a Time-Domain Method. Proceedings of the 20th Symposium on Naval Hydrodynamics, Santa Barbara. California.

Newman. J.N. (1977). Marine Hydrodynamics. The MIT Press, Cambridge, pp. 297.

Newman, J. N. (1978). The Theory of Ship Motions. Advances in Applied Mechanics, Vol. 18, pp. 222-283.

Ogilvie, T. F. (1964). Recent Progress toward the Understanding and Prediction of Ship Motions. Proceedings 5th Symposium on Naval Hydrodynamics, Washington, D.C., pp. 3-128.

Ogilvie, T. F. (1977). Singularity Perturbation Problem in Ship Hydrodynamics. Advances in Applied Mechanics, vol. 17, pp. 91-188.

Ogilvie, T. F. and Tuck, E. O. (1969). A Rational Strip Theory of Ship Motion: Part I. Department of Naval Architecture, The University of Michigan, Report No. 013.

Piegl, L. and Tiller, W. (1987). Curve and Surface Constructions Using Rational B-Splines. Computer-Aided Design, Vol. 19, No. 9, pp. 485-498.

Qiu, W. and Hsiung, C. C. (1999). Theoretical Manual for SEALOADS - A Computer Program for Prediction of Nonlinear Ship Motion, Sea Load and Pressure Distribution in the Time Domain. Technical Report, Centre for Marine Vessel Development and Research, Dalhousie University, Halifax, Nova Scotia, Canada.

Qiu, W., Peng, H. and Hsiung, C. C. (2000). Validation of Time-Domain Prdictions of Motion, Sea Load, and Hull Pressure of a Frigate in Regular Waves. 23rd Symposium on Naval Hydrodynamics, Val de Reuil, France.

Qiu, W. and Hsiung, C. C. (2000). A Panel-Free Method for Time-Domain Analysis of Radiation Problem. Journal of Ocean Engineering, accepted for publication.

Qiu, W., Peng, H. and Hsiung, C. C. (2001a). Enhancement of Wave Loads Prediction by a 3D Time-Domain Code SEALOADS. Martec Limited, Halifax, Nova Scotia, Canada.

Qiu, W., Peng, H. and Hsiung, C. C. (2001b). Computation of Wave Induced Motion and Load Based on Varied Wetted Surface. PRADS 2001, Shanghai, China.

Qiu, W. and Hsiung, C. C. (2001). Time-Domain Analysis of Diffraction Problem by a Panel-Free Method. 5th Canadian Hydromechanics and Marine Structure Conference, Vancouver.

Salvesen, N., Tuck, E. O. and Faltinsen, O. (1970). Ship Motions and Sea Loads. Transactions of Society of Naval Architects and Marine Engineers, Vol. 78, pp. 250-287.

Seibet, G. (2000). The Influence of Variable Added Mass and Damping in a Three-Dimensional Time Domain Ship Motion Program. Master's Thesis, Dalhousie University, Halifax, Nova Scotia, Canada.

Stoker, J. J. (1957). Water Wave. International Science Publishers, Inc., New York.

Wehausen, J. V. (1967). Initial Value Problem for the Motion in an Undulating Sea of a Body with Fixed Equilibrium Position. Journal of Engineering Mathematics, Vol. 1, pp. 1-19.

Wehausen, J. V. (1971). The Motion of Floating Bodies. Annual Review of Fluid Mechanics, Vol. 3, pp. 237-268.

Wehausen, J.V. and Laitone, E.V. (1960). Surface Waves. Handbuch der Physik (ed. S. Flügge), Springer-Verlag, Vol. 9.